Journal of Molecular Structure 1265 (2022) 133419

Contents lists available at ScienceDirect

Journal of Molecular Structure

journal homepage: www.elsevier.com/locate/molstr

Photolability of NO in ruthenium nitrosyls with pentadentate ligand induces exceptional cytotoxicity towards VCaP, 22Rv1 and A549 cancer cells under therapeutic condition

Sadananda Kumbhakar[a], Parth Gupta[b], Bishnubasu Giri[a], Arabinda Muley[a], Kalai Selvan Karumban[a], Ashish Misra[b,*], Somnath Maji[a,*]

[a] Department of Chemistry, Indian Institute of Technology, Kandi, Sangareddy, Hyderabad 502284, Telangana, India
[b] Department of Biotechnology, Indian Institute of Technology, Kandi, Sangareddy, Hyderabad 502284, Telangana, India

ARTICLE INFO

Article history:
Received 25 March 2022
Revised 30 May 2022
Accepted 30 May 2022
Available online 1 June 2022

Keywords:
Redox-active ligand
Ruthenium nitrosyls
Electrochemistry
Crystal structures
Photo release
Anticancer activity
In vitro cytotoxicity

ABSTRACT

Pentadentate electron rich MePBITA ligand in $[Ru^{II}(MePBITA)(NO)]^{n+}$ (n = 3, 2 and MePBITA = 1-(6-(1-methyl-1H-benzo[d]imidazol-2-yl)pyridin-2-yl)-N,N-bis(pyridin-2-ylmethyl)methanamine) permits the isolation of both the redox states of nitrosyls with Enemark–Feltham notation $\{RuNO\}^6$ and $\{RuNO\}^7$. The nitrosyl derivative $[Ru^{II}(MePBITA)(NO)](ClO_4)_3$: $[\mathbf{4}](ClO_4)_3$ was synthesized by stepwise synthetic manner from the chloro precursor $[Ru^{II}(MePBITA)(Cl)](PF_6)$: $[\mathbf{1}](PF_6)$, via the acetonitrile derivative $[Ru^{II}(MePBITA)(CH_3CN)](PF_6)_2$: $[\mathbf{2}](PF_6)_2$ followed by nitro complex $[Ru^{II}(MePBITA)(NO_2)](PF_6)$: $[\mathbf{3}](PF_6)$. All the complexes were fully characterized by different analytical and spectroscopic techniques. Single crystal X-ray structures of the complexes $[\mathbf{1}](PF_6)$, $[\mathbf{2}](PF_6)_2$, $[\mathbf{3}](PF_6)$, and $[\mathbf{4}](ClO_4)_3$ were profitably determined for understanding the molecular integrity. Ru–NO stretching frequency observed at 1931 cm^{-1} for $[\mathbf{4}](ClO_4)_3$ suggests a moderately electrophilic character of NO. The huge shift in ν_{NO} frequency, $\Delta\nu$ (solid) = 325 cm^{-1} was observed by reducing $[\mathbf{4}](ClO_4)_3$ to $[\mathbf{4}](ClO_4)_2$. The conversion of $[\mathbf{3}]^+$ from $[\mathbf{4}]^{3+}$ was examined both electrochemically and spectrophotometrically with the addition of 0.5 M NaOH solution. Rate constants of the first order photorelease (k_{NO}) have been found to be 8.99×10^{-3} min^{-1}; half-life ($t_{1/2}$) = 77 min and 3.84×10^{-2} min^{-1}; half-life ($t_{1/2}$) = 18 min for $[\mathbf{4}]^{3+}$ and $[\mathbf{4}]^{2+}$, respectively with visible Xenon light (200 W) source. The photo liberated NO has been scavenged by biologically relevant target protein reduced myoglobin as Mb–NO adduct. Photoactivation of $[\mathbf{4}]^{3+}$ and $[\mathbf{4}]^{2+}$ by visible light induces significant cytotoxicity in prostate cancer cell lines; VCaP (IC_{50} 29.74 and 4.42 μM) and 22Rv1 (IC_{50} 29.96 and 6.88 μM), and lung cancer cell line; A549 (IC_{50} 2.24 and 0.12 μM). Collectively our results pave the way for the development of metallodrugs as potential therapeutics for a variety of cancers. Additionally, our results also demonstrate how ligand modification could enhance the photolability of metal nitrosyl, adding a new dimension for future efficient photoactive metal nitrosyl design.

1. Introduction

The non-innocent behavior and unique coordination chemistry of nitric oxide (NO) has insisted researchers to explore its role in different physiological and biological environments [1–3]. A small molecule of only two hetero atoms having a considerable electronegativity difference, the emergence of singly occupied molecular orbital (SOMO) justifies its switching between the three possible redox states: radical $NO^{\bullet}$, cationic NO^+, anionic NO^-. This helps in facilitating different coordination modes and within the same architecture, different oxidation states of the central metal atom [4–6]. NO plays important role in cardiovascular control, neuro-transmittance, signalling, and immunology [7–9]. NO is well known to possess anti-cancer properties and its properties have been widely studied in numerous human cancers including breast and colorectal cancers [10]. Studies have revealed that NO induces oxidative stress in cells leading to DNA damage which in turn upregulates the tumor suppressor p53 leading to cell cycle arrest [10,11]. The oxidative and nitrosative effects of NO damage DNA (deamination of nitrogenous bases) and alter the function of a large number of proteins (nitration of amino acids), leading to impaired cellular metabolism and respiration which eventually results in cells undergoing apoptosis.

* Corresponding author.
E-mail addresses: ashishmisra@bt.iith.ac.in (A. Misra), smaji@chy.iith.ac.in (S. Maji).

https://doi.org/10.1016/j.molstruc.2022.133419
0022-2860/

In the human body the heme-containing enzyme NO synthase (NOS) catalyzes L-arginine to synthesize nitric oxide; mainly responsible for physiological disorders if it is deficient in cells. The major drawback of NO-based drugs (such as glyceryl trinitrate) in site-specific NO delivery is the inexorability of NO release from the NO donors. The use of nitrosyls as potential therapeutic agents has increased the demand in the pharmaceutical fields manyfold. Moreover, in the field of photo-chemotherapy (PCT), the controlled release of NO to specific sites has opened a new dimension of nitrosyl chemistry. Metal nitrosyls could be a promising metallodrug due to their controlled photorelease behavior. Light-induced metallodrug activation for site-specific efficient release of active species has been triggered in response to a significant disadvantage of contemporary chemotherapy: weak selectivity towards damaged cells over healthy tissues. Despite the considerable library of metal nitrosyls reported, an appropriate design of ligands framework for versatile applications in pro-drug potentiality, and photodynamic therapy (PDT) become a critical area of interest for researchers till now [12–16]. Most of the iron (Fe) and ruthenium (Ru) nitrosyl complexes have demonstrated effective results in photorelease investigations in the present literature. Even though Fe–nitrosyl complexes have a faster photorelease of NO with low-energy light than Ru–nitrosyl complexes, their instability in an aqueous solution has limited their use in PDT investigations [17–19]. Generally, in aqueous medium, Ru–nitrosyl complexes are not labile, and high-energy UV radiation is necessitated for light-induced release of NO from the metal center, raising another concern for activity in biological conditions [20–22].

The efforts to synthesize ruthenium-nitrosyls with pentadentate ligands commenced a decade ago by Mascharak et al. with the famous $PaPy_3H$ ligand and a series of complexes have been studied comprehensively with different electronic environments [17,23]. Also, photolability and stability were explored extensively. The ligand 1-(6-(1H-benzo[d]imidazol-2-yl)pyridin-2-yl)-N,N-bis(pyridin-2-ylmethyl)methanamine (PBITA) was synthesized previously by Zijian Guo et al. in 2009 and the corresponding zinc complex has been prepared to study as a ratiometric sensor. The intracellular Zn^{2+} imaging ability was investigated with the help of confocal microscope [24]. Consequently, the same group explored the modified PBITA ligand for the ratiometric fluorescent probe for Cd^{2+} and found picomolar detection limit in aqueous media and living cells [25]. Benzimidazole derived ligands have long history in the coordination chemistry and this has been used as a ligand for transition metal ions for the synthesis of DNA cleaving reagents [26–30]. To the best of our knowledge, there is no report of ruthenium complex with PBITA ligand till date and in this study, we have developed methyl substituted PBITA coordinated ruthenium nitrosyl complexes as potential metallodrugs for prostate and lung cancer upon visible light irradiation.

Herein, we have synthesized and stabilized both $\{RuNO\}^6$ and $\{RuNO\}^7$ states with Enemark–Feltham notation [31] in $[Ru^{II}(MePBITA)(NO)]^{n+}$ framework; (MePBITA = 1-(6-(1-methyl-1H-benzo[d]imidazol-2-yl)pyridin-2-yl)-N,N-bis(pyridin-2-ylmethyl)methan amine and n = 3, 2) (Scheme 1). We have demonstrated the synthesis and characterization of $[Ru^{II}(MePBITA)(NO)](ClO_4)_3$: [**4**]$(ClO_4)_3$ along with its precursor metal complexes chloro $[Ru^{II}(MePBITA)(Cl)](PF_6)$: [**1**]$(PF_6)$, acetonitrile $[Ru^{II}(MePBITA)(CH_3CN)](PF_6)_2$: [**2**]$(PF_6)_2$ and nitro $[Ru^{II}(MePBITA)(NO_2)](PF_6)$: [**3**]$(PF_6)$. In addition, we have synthesized the reduced radical species $[Ru^{II}(MePBITA)(NO^{\bullet})](ClO_4)_2$: [**4**]$(ClO_4)_2$ chemically and electrochemically. For all the synthesized metal complexes, the redox and spectral behavior have been carefully studied. Single crystal X-ray structure of the complexes [**1**](PF_6), [**2**]$(PF_6)_2$, [**3**](PF_6) and [**4**]$(ClO_4)_3$ have been profitably determined. The EPR study was carried out at room temperature for one electron reduced species [**4**]$(ClO_4)_2$. The photorelease kinetics have been investigated thoroughly for both [**4**]$(ClO_4)_3$ and [**4**]$(ClO_4)_2$ and the photo liberated NO has been scavenged by biologically relevant target protein, reduced myoglobin as Mb−NO adduct. Furthermore, we examined the cytotoxic properties of nitrosyl complexes, [**4**]$(ClO_4)_3$ and [**4**]$(ClO_4)_2$ which release the coordinated NO upon photoactivation by visible light in human prostate carcinoma cell lines; VCaP and 22Rv1, and lung carcinoma cell line; A549 (see supporting information).

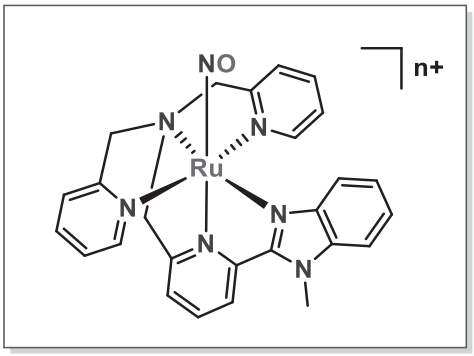

$$\{NO^{+} \longrightarrow (4^{3+})\ NO^{\bullet} \longrightarrow (4^{2+})\}$$

Scheme 1. Molecular framework of nitrosyl $[Ru^{II}(MePBITA)(NO)]^{n+}$: [**4**]$^{3+}(NO^{+})$; [**4**]$^{2+}$ $(NO^{\bullet})$

2. Experimental

2.1. Materials

Pyridine 2,6-dicarboxylic acid and *o*-phenylene diamine were purchased from Avra chemicals (INDIA), isopropyl alcohol, DPA, $RuCl_3{\bullet}3H_2O$ were purchased from Sigma Aldrich. Dimethyl formamide and methyl iodide were purchased from SRL chemicals. All the chemicals and solvents were used without further purification. NMR solvents d_6-DMSO and $CDCl_3$ were purchased from Sigma Aldrich. HPLC grade and dry acetonitrile were used for spectroscopic and electrochemical studies, respectively. The ligand PBITA was synthesized following the reported literature procedure with slight modification [25]. The precursor complex $[Ru^{II}(MePBITA)(Cl)](PF_6)$; [**1**]$(PF_6)$ was synthesized by refluxing the ligand, MePBITA with $RuCl_3{\bullet}3H_2O$ in ethanol solvent under Ar atmosphere. Human prostate carcinoma epithelial cell lines VCaP and 22Rv1, and lung carcinoma epithelial cell line A549 were procured from American Type Culture Collection (ATCC®). Dimethyl sulfoxide (DMSO), formaldehyde solution, crystal violet powder, and NP-40 were purchased from Sigma-Aldrich (Merck). Cell culture media–DMEM and RPMI, tissue culture plates, 4,6-diamidino-2-phenylindole (DAPI), 3-(4,5-dimethylthiazol-2-yl)-2,5-diphenyltetrazolium bromide (MTT reagent), methanol, isopropanol, and hydrochloric acid were obtained from Thermo Fisher Scientific. Fetal bovine serum (FBS) was procured from VWR, Avantor. Penicillin-Streptomycin antibiotic solution was purchased from Lonza.

2.2. Physical measurements

All experiments were carried out in STP laboratory environment under Ar atmosphere. The solvents used such as ethyl acetate, hexane, dichloromethane, and chloroform were distilled following standard laboratory protocol. ^{1}H NMR and ^{13}C NMR spectra were collected at 298 K on Bruker AVANCE III-400 MHz spectrometer in dry, degassed $CDCl_3$ and DMSO-d_6 solvents following standard methods. High-resolution mass spectra (HR-MS) were

recorded in Q-TOF electron spray ionization (ESI) and atmospheric pressure chemical ionization (APCI) modes (Model: HRMS Q-TOF 6538). Electronic spectra were recorded on JASCO V-730 spectrophotometer in CH_3CN at 298 K. Cyclic voltammetric measurements (CV) and differential pulse voltammetry (DPV) analysis were carried out on CHI-660 potentiostat. Electrochemical experiments were performed with a working electrode (3 mm glassy carbon); counter electrode (platinum wire), and a reference electrode (saturated calomel electrode (SCE)) under an Ar atmosphere in the standard three-electrode configuration with a scan-rate at 100 mVs^{-1}. Supporting electrolyte, TBAP (tetra butyl ammonium perchlorate), was used after dissolving the complexes in CH_3CN and the concentration of the solution was $\sim 10^{-3}$ M. The electrical conductivity of all the complexes was measured on Systronic Conductivity bridge 306. FT-IR spectra were recorded on Fourier transform Bruker Alpha-P spectrometer. Single X-ray crystal structures were measured on a Bruker D8 Venture instrument with a Photon III mixed mode detector with graphite-monochromatic Mo-Kα (λ = 0.71073Å) radiation. Elemental analyses were recorded on a BRUKER EURO EA. EPR spectrum was recorded on a JOEL EPR spectrometer. A Thermo Fisher Scientific Steri Cycle CO_2 incubator was used to culture VCaP, 22Rv1, and A549 cell lines. Live-cell and fluorescence imaging were carried out using Nikon ECLIPSE TS2R-FL Inverted Research Microscope. Crystal violet staining images were captured using Bio-Rad Chemidoc XRS$^+$ imaging system. Cell cytotoxicity was measured as absorbance at 595 nm using iMark microplate reader (Bio-Rad).

2.3. Synthesis

2.3.1. Synthesis of 1-(6-(1-methyl-1H-benzo[d]imidazol-2-yl)pyridin-2-yl)-N,N-bis(pyridin-2-ylmethyl)methanamine (MePBITA)

1-(6-(1H-benzo[d]imidazol-2-yl)pyridin-2-yl)-N,N-bis(pyridin-2-ylmethyl)methanamine (PBITA) (0.500 g, 1.23 mmol) was dissolved in 20 mL dry DMF in a doubled neck round bottom flask under argon atmosphere and placed in an ice-water bath. Then, NaH (0.032 g, 1.35 mmol) was carefully added in portion to the stirring solution at 0 °C and allowed to react for half an hour for deprotonation. Then methyl iodide (0.084 mL, 1.35 mmol) was added dropwise to this reaction mixture. After completion of the reaction, it was quenched slowly with ice and water. Then the mixture was washed with brine solution and extracted with EtOAc and dried over anhydrous Na_2SO_4. The solvent was removed under reduced pressure. The residue was purified by column chromatography using silica gel column with (EtOAc: MeOH = 50:1, R_f = 0.35) as eluent afforded pure MePBITA as an off-white gummy liquid. Yield: 413 mg (79.84%). ESI$^+$-MS: *m/z* $[M+H]^+$: calcd. 421.21, found 421.21. ^{1}H NMR (400 MHz, $CDCl_3$): δ (ppm) 8.54 (d, J = 4.8 Hz, 2H), 8.25 (d, J = 7.7 Hz, 1H), 7.88–7.75 (m, 2H), 7.63 (dt, J = 26.5, 7.7 Hz, 5H), 7.43 (d, J = 8.7 Hz, 1H), 7.40–7.28 (m, 2H), 7.21–7.10 (m, 2H), 4.27 (s, 3H), 3.98 (s, 2H), 3.95 (s, 4H). ^{13}C NMR (101 MHz, $CDCl_3$): δ 159.28, 158.36, 150.21, 149.84, 149.07, 142.45, 137.24, 136.44, 123.21, 123.00, 122.96, 122.83, 122.51, 122.07, 119.91, 109.84, 60.40, 60.17, 32.78. FT-IR (solid): 3051, 2923, 2852, 1674, 1589, 1470, 1432, 1387, 1328, 1261, 1152, 1077, 995, 816, 745 cm^{-1}. *Anal calc.* (%) for $[C_{26}H_{24}N_6]$: C 74.26, H 5.75, N 19.99; Found (%): C 73.98, H 5.80, N 19.83.

2.3.2. Synthesis of $[Ru^{II}(MePBITA)(Cl)](PF_6)$ [1](PF_6)

The ligand MePBITA (0.200 g, 0.475 mmol) was dissolved with ethanol, and $RuCl_3 \bullet 3H_2O$ (0.124 g, 0.475 mmol) was added. The mixture was refluxed for 4 h under an argon saturated atmosphere. The initial dark brown color solution changed to deep red color after 1 h. The solvent was removed by using a rotary evaporator to form a dry mass which was dissolved in a minimal amount of methanol. A few drops of saturated aqueous KPF_6 were added to form a dark red precipitate. After filtration, the solid product was washed with cold water and dried in a desiccator. The crude product was further purified by column chromatography using a neutral alumina column and the red band was eluted with 5% MeOH/CH_2Cl_2 as eluent. The solvent was then concentrated in vacuo to afford the desired pure product [**1**](PF_6). Yield: 287 mg (86%). ESI$^+$-MS: *m/z* calcd. 557.08, found 557.07. Molar conductivity [$\Lambda_M(\Omega^{-1}$ cm^2 $M^{-1})$] in CH_3CN at 298 K: 114. ^{1}H NMR (400 MHz, d_6-DMSO): δ (ppm) 8.56 (d, J = 8.1 Hz, 1H), 8.39 (d, J = 8.2 Hz, 1H), 8.02 (d, J = 8.3 Hz, 1H), 7.68–7.59 (m, 4H), 7.84–7.43 (m, 3H), 7.27 (d, J = 7.7 Hz, 1H), 7.18 (d, J = 16.8 Hz, 2H), 6.97–6.94 (m, 2H), 5.11 (d, J = 14.8 Hz, 2H), 4.97 (t, J = 7.4 Hz, 4H), 4.47 (s, 3H). FT-IR (solid): $\nu(PF_6^-)$, 842.55 cm^{-1}. *Anal calc.* (%) for $[C_{26}H_{24}ClF_6N_6PRu]$: C 44.48, H 3.45, N 11.97; Found (%): C 44.45, H 3.49, N 11.92.

2.3.3. Synthesis of $[Ru^{II}(MePBITA)(CH_3CN)](PF_6)_2$ [2]$(PF_6)_2$

The pure chloro complex [**1**](PF_6) (0.250 mg, 0.356 mmol) was dissolved in 20 mL water/ acetonitrile mixture (1:1, v/v), in a round bottom flask and refluxed under argon saturated atmosphere for 12 h. The initial deep red colored solution changed to reddish orange. Then the solution was cooled down and mixture was evaporated to a minimum volume. A few drops of aqueous saturated KPF_6 solution were added to afford orange color precipitate. The precipitate was filtered off, washed twice (5 mL × 2) with ice cold H_2O, and dried in desiccator. The crude product then purified by flash chromatography using a neutral alumina column with 20% CH_3CN/CH_2Cl_2 as eluent to obtain the pure product [**2**]$(PF_6)_2$ as orange solid. Yield: 231 mg (76.10%). ESI$^+$-MS: *m/z* calcd. 853.07, found 853.46. Molar conductivity [$\Lambda_M(\Omega^{-1}$ cm^2 $M^{-1})$] in CH_3CN at 298 K: 235. ^{1}H NMR (400 MHz, d_6- DMSO): δ (ppm) 8.50 (d, J = 8.2 Hz, 1H), 8.12 (d, J = 8.4 Hz, 1H), 7.92 (dd, J = 14.2, 8.1 Hz, 2H), 7.78 (t), J = 7.7 Hz, 2H), 7.69 (t, J = 7.7 Hz, 1H), 7.57 (dd, J = 14.2, 7.4 Hz, 3H), 7.42 (d, J = 7.9 Hz, 1H), 7.25 (d, J = 5.2 Hz, 2H), 7.05 (t, J = 6.4 Hz, 2H), 5.25–5.12 (m, 4H), 5.08 (s, 2H), 4.49 (s, 3H), 2.71 (s, 3H). FT-IR (solid): $\nu(PF_6^-)$, 836.55 cm^{-1}. *Anal calc.* (%) for $[C_{28}H_{27}F_{12}N_7P_2Ru]$: C 39.45, H 3.19, N 11.50; Found (%): C 39.44, H 3.23, N 11.46.

2.3.4. Synthesis of $[Ru^{II}(MePBITA)(NO_2)](PF_6)$ [3](PF_6)

The acetonitrile derivative [**2**]$(PF_6)_2$ (160 mg, 0.18 mmol) was dissolved in an acetone/water (1:1 v/v) mixture and excess sodium nitrite ($NaNO_2$) (192 mg, 2.78 mmol) was added. The solution was refluxed for 12 h. The initial orange color solution changed to brownish red. Acetone was removed by a rotary evaporator and the microcrystalline solid was filtered off, washed thrice (5 mL × 3) with ice cold H_2O, and dried in desiccator. Yield: 106 mg (80%). ESI$^+$-MS: *m/z* calcd. 568.10, found 568.10. Molar conductivity [$\Lambda_M(\Omega^{-1}$ cm^2 $M^{-1})$] in CH_3CN at 298 K: 137. ^{1}H NMR (400 MHz, d_6- DMSO): δ (ppm) 8.46 (d, J = 8.1 Hz, 1H), 8.05 (d, J = 8.5 Hz, 1H), 7.99 (d, J = 8.1 Hz, 1H), 7.86 (t, J = 8.0 Hz, 1H), 7.71 (d, J = 9.2 Hz, 2H), 7.62 (t, J = 8.2 Hz, 1H), 7.51–7.42 (m, 3H), 7.38 (d, J = 7.8 Hz, 1H), 7.24 (d, J = 5.4 Hz, 2H), 7.01 (t, J = 6.4 Hz, 2H), 5.04 (d, J = 6.0 Hz, 4H), 4.97 (d, J = 15.3 Hz, 2H), 4.48 (s, 3H). FT-IR (solid): $\nu(PF_6^-)$, 842.55, $\nu(NO_2^-)$, 1419.3, 1288.2 cm^{-1}. *Anal calc.* (%) for $[C_{26}H_{24}F_6N_7O_2PRu \cdot CH_3OH]$: C 43.55, H 3.79, N 13.17; Found (%): C 43.53, H 3.83, N 13.11.

2.3.5. Synthesis of $[Ru^{II}(MePBITA)(NO)](ClO_4)_3$ [4]$(ClO_4)_3$

Conc. HNO_3 (0.5 mL) was added dropwise to the solid [**3**](PF_6) (70 mg, 0.098 mmol) at 0 °C to get a pasty mass under constant stirring. After that, conc. $HClO_4$ (2 mL) was added very carefully under same condition. After that a few drops of saturated aqueous $NaClO_4$ was added to form yellow precipitate. The precipitate was filtered off and the solid product was washed with ice

cold water and dried in desiccator under argon saturated atmosphere. Yield: 61 mg (73.23%). ESI$^+$-MS: *m/z* calcd. 848.95, found 848.91. Molar conductivity [$\Lambda_M(\Omega^{-1}$ cm^2 M$^{-1})$] in CH_3CN at 298 K: 341. ^{1}H NMR (400 MHz, d_6-DMSO): δ (ppm) 8.78 (d, J = 8.2 Hz, 1H), 8.45 (t, J = 8.1 Hz, 1H), 8.30 (ddd, J = 10.7, 9.1, 4.8 Hz, 3H), 8.04 (d, J = 7.8 Hz, 2H), 7.97 (d, J = 8.1 Hz, 1H), 7.84 (t, J = 7.4 Hz, 1H), 7.78 (t, J = 8.2 Hz, 1H), 7.74 (d, J = 8.1 Hz, 1H), 7.69 (d, J = 5.8 Hz, 2H), 7.52 (t, J = 6.6 Hz, 2H), 5.87 (d, J = 18.1 Hz, 4H), 5.74 (d, J = 16.1 Hz, 2H), 4.53 (s, 3H). FT-IR (solid): $\nu(ClO_4^-)$, 1095. $\nu(NO^+)$, 1931 cm^{-1}. *Anal calc.* (%) for [$C_{26}H_{24}Cl_3N_7O_{13}Ru$]: C 36.74, H 2.85, N 11.54; Found (%): C 36.75, H 2.88, N 11.49.

2.3.6. Synthesis of [Ru^{II}(MePBITA)(NO$^\bullet$)](ClO$_4$)$_2$ [4](ClO$_4$)$_2$

[4]$(ClO_4)_3$ (30 mg, 0.035 mmol) was dissolved in 2 mL acetone and excess hydrazine hydrate was added. The solution was stirred for 15 min under argon saturated atmosphere. The yellow color solution readily changed to dark color. After removal of solvent the dark precipitate was washed with ice cold water. It was then dried in a desiccator under argon saturated atmosphere. Yield: 17 mg (64.71%). ESI$^+$-MS: *m/z* calcd. 750.01, found 750.12. FT-IR (solid): $\nu(ClO_4^-)$, 1085, $\nu(NO^\bullet)$, 1606 cm^{-1}.

Caution! Perchloric acid and metal perchlorates are explosive. Proper precautions should be taken while handling and recommended to use in minimal quantity.

2.4. Scavenging of photo-liberated NO by myoglobin (Mb)

In a quartz cuvette 3 mL CH_3CN solution of [**4**]$(ClO_4)_3$ was taken and sealed properly to make air-tight, then it was degassed fully with an argon atmosphere. Then the cuvette was exposed with visible 200 W Xenon light for photolysis ($\sim$ 2 h). Afterwards the photo released NO gas passed with the help of a cannula into a freshly prepared aqueous solution of reduced myoglobin. Finally, the electronic absorption spectra were recorded. For the reduced radical species [**4**]$(ClO_4)_2$ the same experiment was replicated and the duration was $\sim$ 80 min.

2.5. Crystallography

Single crystals of [**1**](PF_6), [**2**]$(PF_6)_2$, [**3**](PF_6) and [**4**]$(ClO_4)_3$ were grown by slow evaporation in dichloromethane/methanol (9:1), acetonitrile, dichloromethane/methanol (8:2) and acetonitrile solvent, respectively. Suitable crystals were chosen for each of the complexes and cut properly prior to the measurement. The data were collected in Bruker D8 Venture instrument with a Photon III mixed mode detector with graphite-monochromatic Mo-Kα (λ = 0.71073Å) radiation. Selected suitable crystal was mounted on a CryoLoop (Hampton Research Corporation) by applying a layer of mineral oil. The structure was solved by direct methods (SIR2004) and refined on F^2 by using SHELXL [32] using OLEX2 [33]. All hydrogen atoms were situated at the calculated positions, and all atoms along with non-hydrogen atoms were refined anisotropically. The MERCURY program was used for drawing the molecules. For this paper CCDC numbers 2106537, 2106538, 2106539 and 2106540 for [**1**](PF_6), [**2**]$(PF_6)_2$, [**3**](PF_6) and [**4**]$(ClO_4)_3$, respectively contain the supplementary crystallographic data.

2.6. Cell culture

Human prostate adenocarcinoma cell line: VCaP was established from osteocytes of a 59-year-old male suffering from hormone-refractory prostate cancer metastasized to the bones and lung adenocarcinoma cell line; A549 was derived from lung tissue of a patient with lung cancer were cultured in Dulbecco's Modified Eagle Medium (Gibco) with the addition of 10% FBS (VWR) and 1% Penicillin-Streptomycin antibiotic solution (Lonza). Prostate carcinoma epithelial cell line 22Rv1 was maintained in RPMI 1640 medium (Gibco) supplemented with 10% FBS and 1% antibiotic solution. These cell lines were specifically chosen for their ability to closely mimic human tumor physiology. Depending on the experiments, these cells were seeded either in 12-well and/or 96-well plates (Thermo Fisher Scientific) and were cultured in humid conditions with a constant 5% CO_2 at 37 °C [34].

2.7. Live-cell and fluorescence imaging experiments

Cancer cells: VCaP, 22Rv1, and A549 were separately seeded in 12-well plates with 10^4 cells/well density to observe the effects of all ruthenium derivatives and cultured in their respective supplemented media at 37 °C in a 5% CO_2 incubator. All the complexes were dissolved in 100% DMSO for further use. The working dilutions of compounds were prepared in such a way that the final concentration of DMSO in each well was ranging between 2-5%. The cells were treated with [**1**](PF_6), [**2**]$(PF_6)_2$, [**3**](PF_6), [**4**]$(ClO_4)_3$, and [**4**]$(ClO_4)_2$ at different concentrations in the dark and cultured for 6 h in abovementioned conditions. Cells treated with 5% DMSO were taken as control. Afterward, the growth media was removed, and cells were washed multiple times using 1X phosphate-buffered saline (PBS) to remove residual complexes and bright-field images of the cells were captured. Thereafter, PBS was added again, and the cells were photo-exposed for 15 m using a visible light source Xenon (200 W) bulb. Later, PBS was removed, and fresh culture media was added. The cells were again cultured for 24 h. Bright-field images of the cells were captured post-light exposure using Nikon Inverted Research Microscope at 100 ms exposure. After live-cell imaging, cells were stained with 2 µg/ml of a fluorescent DNA stain DAPI, following a protocol adapted from earlier literature [35], to observe the effects of various ruthenium complexes on the nuclear degradation of the cells. Fluorescence imaging was performed using Nikon Inverted Research Microscope at 20 ms exposure. Further, to observe relative cell death, the cells were stained using 0.1% crystal violet dye (prepared in 20% Methanol v/v) and the image was captured using Bio-Rad Chemidoc XRS$^+$ imaging system after multiple washes using 1X PBS to remove the residual dye.

2.8. Cell cytotoxicity experiments

VCaP, 22Rv1, and A549 cells were separately seeded into 96-well plates at a cell density of 10^3 cells/well and cultured for 16 h in their respective supplemented media at 37 °C in a 5% CO_2 incubator. To quantitatively estimate their cytotoxic ability, the cells were treated with our various ruthenium complexes [**1**](PF_6), [**2**]$(PF_6)_2$, [**3**](PF_6), [**4**]$(ClO_4)_3$, [**4**]$(ClO_4)_2$, and cultured for 6 h. Thereafter, the cells were washed multiple times using 1X PBS and were photo-exposed for 15 min using a visible light Xenon (200 W) bulb in PBS. Fresh culture media was then added, and the cells were again cultured for 24 h. Subsequently, 100 µL of 0.5 mg/mL MTT reagent was added to the cells and incubated for 4 h. Afterward, MTT reagent was aspirated and 100 µL MTT solvent (4 mM HCl, 0.1% Nondet P-40 (NP-40) prepared in isopropanol) was added to each well of the 96-well plates and rotated gently for 20 min using an orbital shaker to dissolve formed formazan crystals. Later, absorbance was noted at a wavelength of 595 nm using iMark microplate reader (Bio-Rad). The cellular toxicity of ruthenium complexes was calculated as a ratio of recorded absorbance at 595 nm of treated cells to the 5% DMSO-treated cells as control, and IC_{50} values were determined using GraphPad Prism.

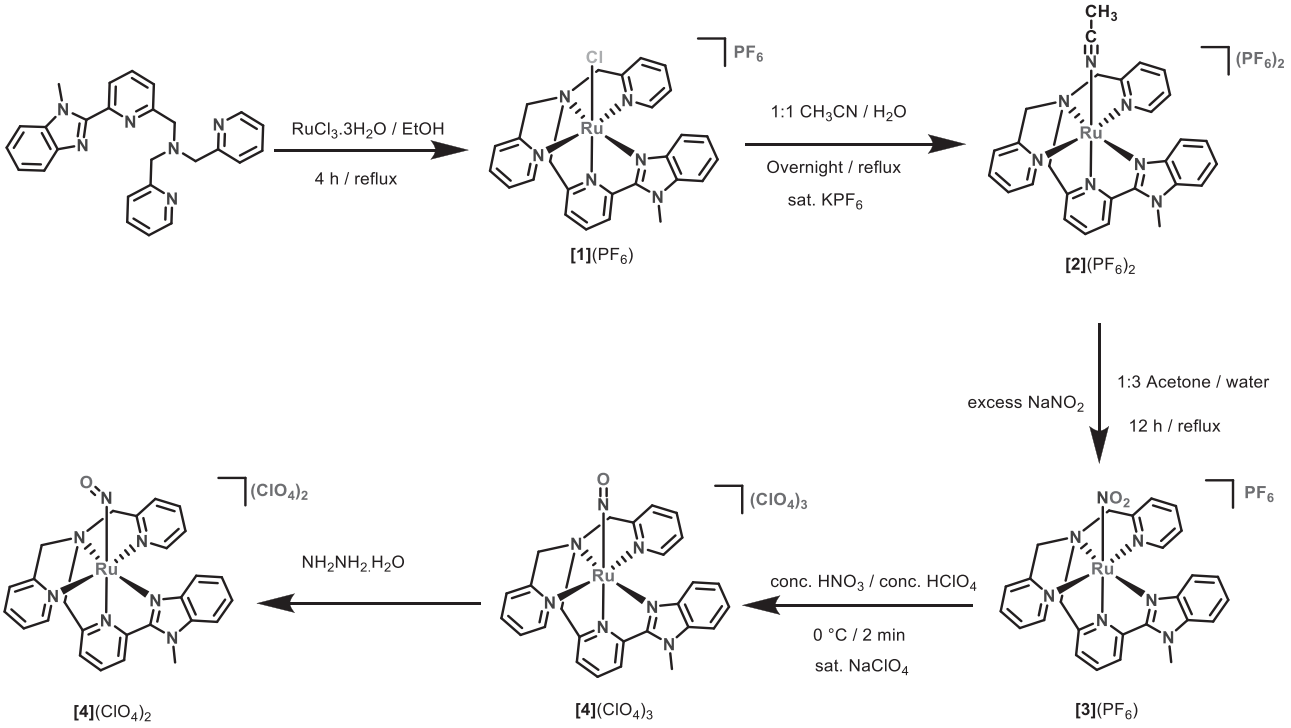

Scheme 2. Synthesis of [**1**](PF_6), [**2**]$(PF_6)_2$, [**3**](PF_6), [**4**]$(ClO_4)_3$ and [**4**]$(ClO_4)_2$.

3. Results and discussion

3.1. Synthesis and characterization

The pentadentate ligand PBITA was synthesized following the previously reported literature procedure [25]. The targeted 1-(6-(1-methyl-1*H*-benzo[*d*]imidazole-2-yl)pyridine-2-yl)-*N*,*N*-bis(pyridine-2-ylmethyl)methanamine (MePBITA) ligand was synthesized by simple methylation of PBITA in DMF. The precursor chloro complex [**1**](PF_6) was synthesized by refluxing the ligand, MePBITA with $RuCl_3{\bullet}3H_2O$ in ethanol. The nitrosyl derivative [**4**]$(ClO_4)_3$ has been prepared by a stepwise synthetic manner from the chloro precursor [**1**](PF_6), via the acetonitrile derivative [**2**]$(PF_6)_2$ followed by nitro complex [**3**](PF_6) (Scheme 2). In spite of several tries, we failed to isolate the pure [**4**]$(ClO_4)_3$ from [**1**](PF_6) or [**2**]$(PF_6)_2$ by direct synthesis utilizing either NO gas or $NOBF_4$ perhaps due to the saturated coordinated environment. The solvate acetonitrile derivative [**2**]$(PF_6)_2$ was prepared by overnight refluxing with water/acetonitrile mixture (1:1, v/v) and the corresponding nitro complex [**3**](PF_6) was synthesized from the acetonitrile precursor [**2**]$(PF_6)_2$ on heating with excess aqueous $NaNO_2$ solution. The nitrosyl complex [**4**]$(ClO_4)_3$ was prepared from the nitro precursor [**3**](PF_6) by using conc. HNO_3 and conc. $HClO_4$ at 0 °C. To avoid any unwanted side reactions, we have used conc. HNO_3 and conc. $HClO_4$. It is well-known that the free NO_2^- can take part in disproportionation reaction forming NO_3^- and NO in presence of acid [36, 37]. By the reduction of [**4**]$(ClO_4)_3$ chemically with hydrazine hydrate, the one-electron reduced [**4**]$(ClO_4)_2$ radical complex was afforded. The formation of [**4**]$(ClO_4)_2$ radical complex was confirmed by EPR spectroscopy g = ~ 2.22, see Fig. 8) suggesting a substantial contribution of ruthenium and nitrosyl singly occupied MO [37,38].

All the complexes were isolated and purified by column chromatography with neutral alumina while the isolation for the nitrosyl derivatives as perchlorate salts. In principle all the complexes showed satisfactory mass spectra, ^1H NMR data, FT-IR data, elemental analysis, and electrical conductivity indicated their formation. The molecular integrity was authenticated by the single crystal structure determination for [**1**](PF_6), [**2**]$(PF_6)_2$, [**3**](PF_6) and [**4**]$(ClO_4)_3$ (Figs. 1–4).

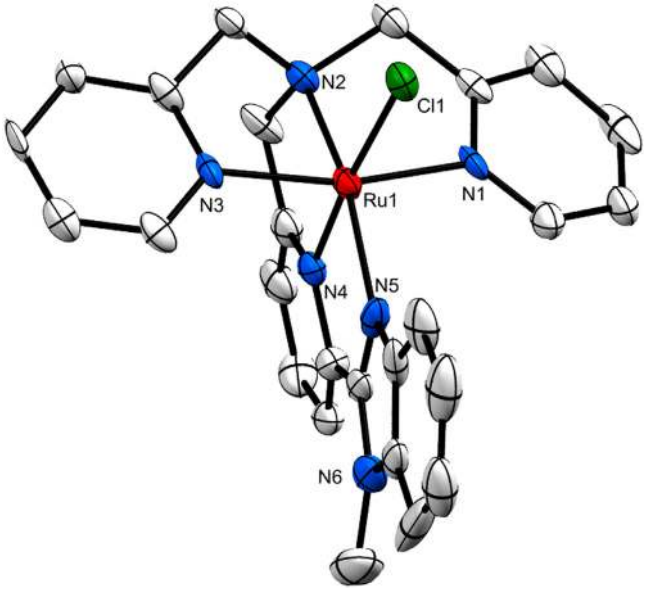

Fig. 1. Molecular structure of the cation $[1]^+$. Ellipsoids are drawn at 40% probability. Hydrogen atoms are omitted for clarity.

3.2. Crystallographic description

Molecular structure of [**1**](PF_6), [**2**]$(PF_6)_2$, [**3**](PF_6), and [**4**]$(ClO_4)_3$ were elucidated by single crystal X-ray diffraction study. Suitable single crystals of [**1**](PF_6) and [**3**](PF_6) were grown by slow evaporation in the mixture of dichloromethane/methanol (9:1) and dichloromethane/methanol (8:2), respectively while for [**2**]$(PF_6)_2$ and [**4**]$(ClO_4)_3$ via slow evaporation in acetonitrile

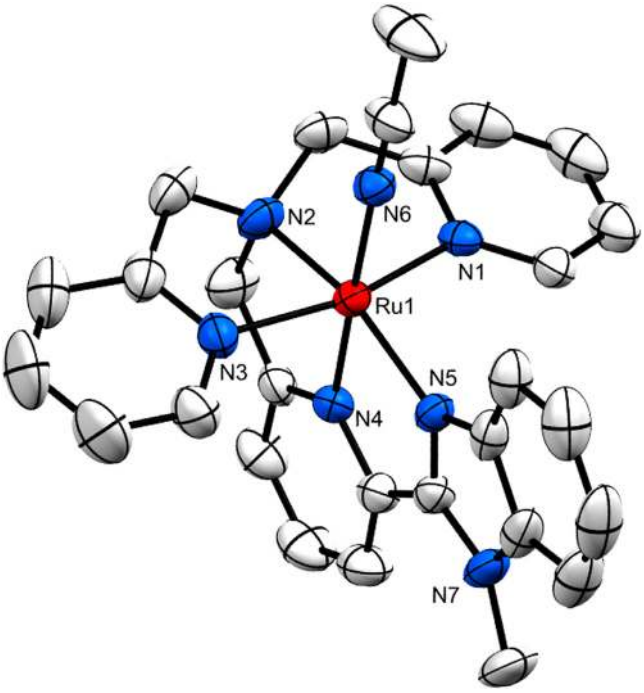

Fig. 2. Molecular structure of the cation $[\mathbf{2}]^{2+}$. Ellipsoids are drawn at 40% probability. Hydrogen atoms are omitted for clarity.

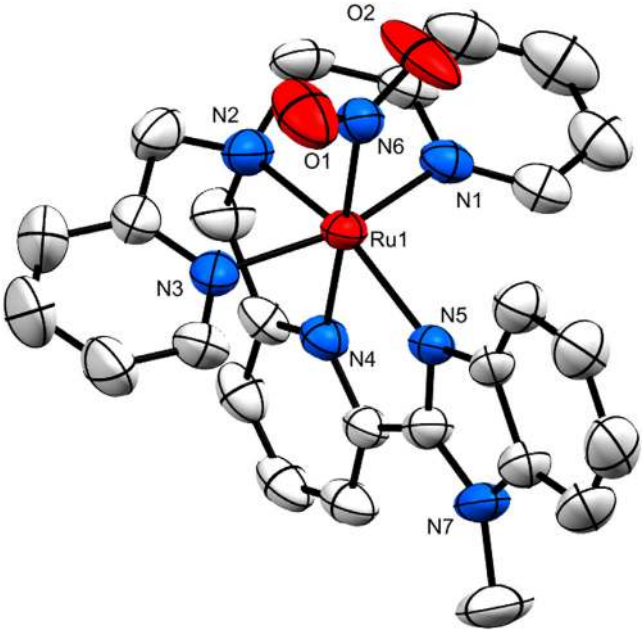

Fig. 3. Molecular structure of the cation $[\mathbf{3}]^{+}$. Ellipsoids are drawn at 40% probability. Hydrogen atoms and solvent molecule are omitted for clarity.

solvent. All of the complexes exhibit distorted octahedral geometry with monoclinic (space group $P2_1/n$), triclinic (space group, *P-1*), monoclinic (space group $P2_1/n$), and orthorhombic (space group, $P2_12_12_1$) crystal system for [**1**](PF_6), [**2**]$(PF_6)_2$, [**3**](PF_6), and [**4**]$(ClO_4)_3$, respectively. Crystallographic parameters and important bond angles (°)/bond distances (Å) are shown in Tables 1 and 2, respectively. The ligand, MePBITA was coordinated to the central ruthenium by their corresponding nitrogen donor atoms, and the remaining axial position was occupied with Cl, CH_3CN, NO_2, and NO for [**1**](PF_6), [**2**]$(PF_6)_2$, [**3**](PF_6), and [**4**]$(ClO_4)_3$, respectively. Bond lengths between central ruthenium ion and the coordinated nitrogen atoms of MePBITA fairly matched with the analogous

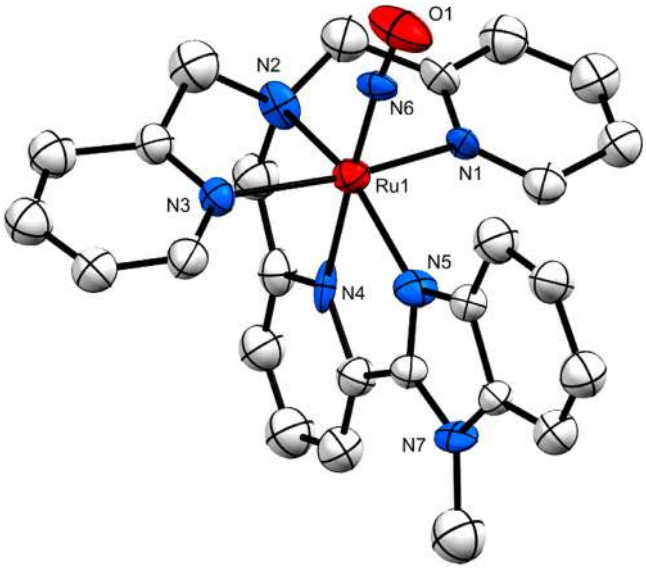

Fig. 4. Molecular structure of the cation $[\mathbf{4}]^{3+}$. Ellipsoids are drawn at 40% probability. Hydrogen atoms are omitted for clarity.

complexes (Table 2) [38–40]. The Ru−N4 bonds between the pyridine imidazole rings and central ruthenium are slightly shorter in comparison to the rest of the Ru−N bonds. Ru−Cl, Ru−CH_3CN, Ru−NO_2, and Ru−NO bond distances were found to be 2.446(4), 2.053(5), 2.043(6) and 1.728(14) Å for [**1**](PF_6), [**2**]$(PF_6)_2$, [**3**](PF_6), and [**4**]$(ClO_4)_3$, respectively. In all the structures the N4–Ru–X (X = Cl, CH_3CN, NO_2 and NO) bond angles are linear ∼180°. The O1−N6−O2 bond angle 112.8(6) ° in [**3**](PF_6) suggested the bending NO_2 coordination. In [**4**]$(ClO_4)_3$ the strong electrophilic character of the NO^+ has been revealed by the N6–O1 bond length of 1.147(14)Å and Ru1–N6–O1 (°) of 175.0(14) like the earlier reported analogous ruthenium nitrosyls. (Table 2 and Fig. 4).

3.3. Spectral analysis

3.3.1. NMR spectral study

The ^1H NMR spectrum in $CDCl_3$ at room temperature of the free ligand MePBITA exhibited all the expected 24 protons that were well resolved; in which 15 aromatic protons were appearing in the region of 8.54−7.14 ppm and the rest 9 aliphatic protons in the region of 3.95−4.27 ppm. The distinct three methyl protons of pyridyl benzimidazole ring appeared at 4.27 ppm and the six methylene protons appeared at 3.95−3.98 ppm. The four methylene protons attached to the bis(pyridine-2ylmethyl)amine (DPA) parts were quite shielded in comparison to the benzimidazole-connected two methylene protons. ^{13}C NMR spectrum in $CDCl_3$ at room temperature of the free ligand MePBITA exhibits the distinct peaks expected for the methyl and methylene groups at 32.78 and 60.17–60.40 ppm, respectively. All the complexes $[\mathbf{1}]^+$, $[\mathbf{2}]^{2+}$, $[\mathbf{3}]^+$ and $[\mathbf{4}]^{3+}$ are diamagnetic in nature as evident from the ^1H NMR spectra recorded in d_6-DMSO at room temperature, revealed the expected 15 aromatic protons in the region of 8.78−6.94 ppm, in which 8 protons from DPA unit and the other 7 protons from the pyridyl benzimidazole unit of MePBITA ligand moiety (Supporting Information, Figs. S1−S6). The signals are quite deshielded compared to the free MePBITA ligand aromatic signals suggesting the successful metalation. In all the complexes trivial changes in the chemical shift values are associated with different axial monodentate (Cl, CH_3CN, NO_2 or NO) ligands. The characteristic singlet for three methyl protons of pyridyl benzimidazole ring that appeared in the region of 4.46−4.53 ppm in all complexes has been perfectly

Table 1
Selected crystallographic parameters for [**1**](PF_6), [**2**](PF_6)$_2$, [**3**](PF_6) and [**4**](ClO_4)$_3$

Complex	[**1**](PF_6)	[**1**](PF_6)$_2$	[**3**](PF_6)	[**4**](ClO_4)$_3$
Empirical formula	$C_{52}H_{48}Cl_2F_{12}N_{12}P_2Ru_2$	$C_{28}H_{26.5}F_{12}N_7P_2Ru$	$C_{53}H_{52}F_{12}N_{14}O_5P_2Ru_2$	$C_{26}H_{24}Cl_3N_7O_{13}Ru$
Formula weight	1404.00	852.07	1457.16	849.94
Temperature/K	101.0	273.15	273.15	273.15
Crystal system	monoclinic	triclinic	monoclinic	orthorhombic
Space group	$P2_1/n$	$P\text{-}1$	$P2_1/n$	$P2_12_12_1$
a/Å	14.904(2)	12.382(3)	15.041(4)	8.5217(12)
b/Å	15.980(2)	16.916(4)	16.171(4)	19.354(2)
c/Å	24.120(3)	18.298(4)	24.654(6)	20.233(2)
α/°	90	107.230(6)	90	90
β/°	94.664(4)	107.343(6)	97.552(8)	90
γ/°	90	99.752(7)	90	90
Volume/Å^3	5725.2(14)	3351.7(12)	5945(3)	3337.0(7)
Z	4	4	4	4
ρ_{calc}g/cm^3	1.629	1.689	1.628	1.692
μ/mm^{-1}	0.764	0.663	0.659	0.785
F(000)	2816.0	1702.0	2936.0	1712.0
Crystal size/mm^3	0.27 × 0.21 × 0.13	0.26 × 0.25 × 0.12	0.27 × 0.26 × 0.12	0.29 × 0.24 × 0.17
Radiation	MoKα (λ = 0.71073)	MoKα (λ = 0.71073)	MoKα (λ = 0.71073)	MoKα (λ = 0.71073)
2θ range for data collection/°	4.016 to 54.732	4.25 to 54.262	3.922 to 54.466	5.186 to 54.136
Index ranges	-19 ≤ h ≤ 19, -20 ≤ k ≤ 20, -29 ≤ l ≤ 31	-15 ≤ h ≤ 15, -21 ≤ k ≤ 21, -23 ≤ l ≤ 20	-19 ≤ h ≤ 19, -20 ≤ k ≤ 20, -31 ≤ l ≤ 31	-7 ≤ h ≤ 10, -18 ≤ k ≤ 24, -18 ≤ l ≤ 25
Reflections collected	101561	62297	63932	12854
Independent reflections	12855 [R_{int} = 0.1382, R_{sigma} = 0.0916]	14720 [R_{int} = 0.0781, R_{sigma} = 0.0639]	13119 [R_{int} = 0.0803, R_{sigma} = 0.0778]	6719 [R_{int} = 0.1761, R_{sigma} = 0.4137]
Data/restraints/parameters	12855/0/742	14720/0/905	13119/0/798	6719/144/452
Goodness-of-fit on F^2	1.090	1.055	1.039	0.823
Final R indexes [I>=2σ (I)]	R_1 = 0.1503, wR_2 = 0.3407	R_1 = 0.0681, wR_2 = 0.1687	R_1 = 0.0702, wR_2 = 0.1761	R_1 = 0.0746, wR_2 = 0.1335
Final R indexes [all data]	R_1 = 0.1929, wR_2 = 0.3650	R_1 = 0.0959, wR_2 = 0.1894	R_1 = 0.1213, wR_2 = 0.1998	R_1 = 0.2351, wR_2 = 0.1767
Largest diff. peak/hole / e Å^{-3}	5.59/-2.28	0.98/-0.82	1.05/-0.62	0.87/-0.55

*Even though data collection was done at low temperature but due to poor quality crystal for [**1**](PF_6) the refinement factor is bit high.

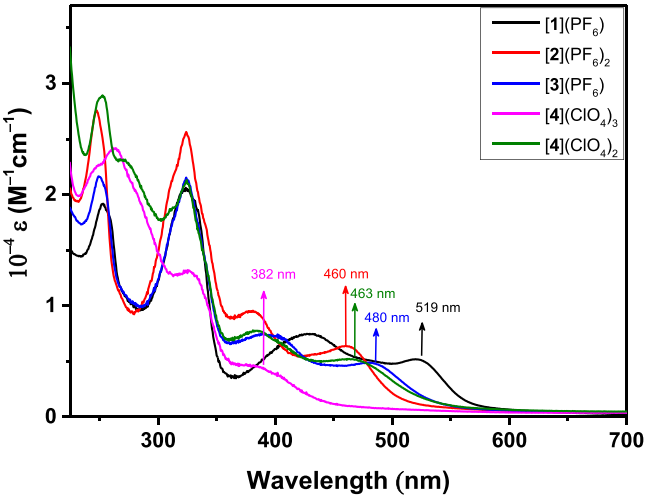

Fig. 5. UV-vis spectra of complex [**1**]$^+$ (black), [**2**]$^{2+}$ (red), [**3**]$^+$ (blue), [**4**]$^{3+}$ (pink) and [**4**]$^{2+}$ (green) in CH_3CN.

identified. The four methylene protons related to the DPA unit of the ligand are appearing more deshielded compared to the free ligand in the region of 4.94–5.89 ppm. The typical sharp singlet peak for the methyl group of coordinated CH_3CN for the solvated complex [**2**]$^{2+}$ appeared at 2.70 ppm.

3.3.2. UV-vis spectroscopy

The complexes exhibit electronic transition around 500 nm which can be attributed to ruthenium(II) based metal to ligand charge transfer (MLCT) transitions to π^* orbitals of ligand MePBITA and ligand-based intense multiple transitions in the high energy UV region (Fig. 5, Table 3) [38].

Due to the different relative stabilization of the dπ(Ru) level surrounded by the different ligand field strengths of X (X = Cl, CH_3CN, NO_2^-, NO^+ and $NO^\bullet$) the MLCT band energy in acetonitrile solution follows the order [**1**] (PF_6) (519 nm) < [**3**](PF_6) (480 nm) < [**4**](ClO_4)$_2$ (463 nm) ≈ [**2**](PF_6)$_2$ (460 nm) < [**4**](ClO_4)$_3$ (382 nm). The complexes [**1**](PF_6) and [**3**](PF_6) show low energy MLCT transitions due to the presence of negatively charged Cl^- and NO_2^- which further indicates the relative destabilization of the dπ(Ru) electrons [41,42]. A noticeable high energy shift of the MLCT band in [**4**](ClO_4)$_3$ implies a strong dπ(Ru^{II}) → π^*(NO^+) back-bonding interaction. The increased electron density around the central ruthenium metal by the strong chelating electron rich MePBITA facilitates an increase in the energy gap between Ru(dπ) and NO^+(π^*). This has further been evidenced in the observed triple bond character short Ru–N8 (NO) bond distance of 1.728(14) Å (Table 2) and the moderately high ν(NO) frequency of 1931 cm^{-1}. But for [**4**](ClO_4)$_2$ the MLCT band is at 463 nm due to the comparable lower band gap between Ru(dπ) and $NO^\bullet$(π^*).

3.3.3. FT-IR spectral analysis

The FT-IR vibrational spectra for $\nu(PF_6^-)$ appears in the expected ~ 840 cm^{-1} and for $\nu(ClO_4^-)$ vibrations ~ 1090 cm^{-1} which is summarized in (Table S1, Figs. S7-S12). For [**3**](PF_6) the typical Ru–NO_2 frequencies are observed at 1288 cm^{-1} and 1324 cm^{-1}, respectively which can be assigned as symmetric and asymmetric stretching vibration (Fig. S10) [37,39,40]. The observed stretching frequency at 1931 cm^{-1} for [**4**](ClO_4)$_3$ suggesting the moderately strong Ru–NO bonding feature of Ru–NO (Table 4 and ligand drawing). In the past ruthenium nitrosyl complexes of nitrogen based pentadentate ligand the observed Ru–NO stretching frequencies are in the range of 1862–1920 cm^{-1} which are relatively lower in comparison with the present [**4**](ClO_4)$_3$ (Table 4). Comparative analysis of the relative Ru–NO stretching frequencies of analogous molecular frameworks $[Ru^{II}(L^5)(NO^+)]^{3+}$; the stretching frequencies values were found to be 1920, 1899, 1877, and 1862 cm^{-1} for $[Ru^{II}(SBPy_3)(NO^+)]^{3+}$, $[Ru^{II}(PaPy_3)(NO^+)]^{2+}$, $[Ru^{II}(Py_3P)(NO^+)]^+$, and $[Ru^{II}(Py_3P)(NO^+)(Cl)]$, respectively. In [**4**](ClO_4)$_3$ the DPA

Table 2
Selected bond length (Å) and bond angles (°) for [**1**](PF_6), [**2**](PF_6)$_2$, [**3**](PF_6) and [**4**](ClO_4)$_3$

Bond length / Bond angle	[**1**](PF_6)	[**2**](PF_6)$_2$	[**3**](PF_6)	[**4**](ClO_4)$_3$
Ru1–N1	2.070(10)	2.065(4)	2.062(6)	2.087(13)
Ru1–N2	2.070(12)	2.074(4)	2.068(6)	2.074(12)
Ru1–N3	2.054(10)	2.069(5)	2.057(6)	2.072(14)
Ru1–N4	1.981(12)	1.974(4)	1.998(5)	2.027(13)
Ru1–N5	2.098(11)	2.080(4)	2.088(5)	2.113(15)
Ru1–N6	–	2.053(5)	2.043(6)	1.728(14)
Ru1–Cl1	2.446(4)	–	–	–
N6–O1	–	–	1.236(8)	1.147(14)
N6–O2	–	–	1.211(7)	–
Ru2–N7	2.065(16)	–	–	–
Ru2–N8	2.059(12)	2.082(4)	2.072(5)	–
Ru2–N9	2.043(13)	2.065(5)	2.094(5)	–
Ru2–N10	1.959(12)	2.061(5)	2.088(5)	–
Ru2–N11	2.101(11)	1.976(4)	1.998(5)	–
Ru2–N12	–	2.070(5)	2.088(5)	–
Ru2–N13	–	2.052(5)	2.030(5)	–
Ru2–Cl2	2.446(4)	–	–	–
N13–O3	–	–	1.206(7)	–
N13–O4	–	–	1.246(7)	–
N1–Ru1–N2	82.0(5)	81.97(19)	80.9(2)	80.1(5)
N1–Ru1–N3	163.5(5)	163.82(19)	164.0(2)	162.1(6)
N1–Ru1–N4	86.4(4)	88.89(17)	90.8(2)	86.9(5)
N1–Ru1–N5	98.5(5)	98.55(17)	99.6(2)	97.8(5)
N1–Ru1–N6	–	89.22(17)	90.9(2)	93.5(6)
N1–Ru1–Cl1	90.2(3)	–	–	–
N2–Ru1–N3	81.6(5)	81.9(2)	83.1(3)	82.6(6)
N2–Ru1–N4	84.2(5)	83.38(19)	83.3(2)	81.7(6)
N2–Ru1–N5	161.7(5)	162.12(19)	160.9(2)	158.7(5)
N2–Ru1–N6	–	96.01(19)	96.2(2)	101.7(6)
N2–Ru1–Cl1	97.8(3)	–	–	–
N3–Ru1–N4	93.4(4)	89.72(18)	89.2(2)	86.0(5)
N3–Ru1–N5	97.6(4)	96.98(18)	96.0(2)	96.7(6)
N3–Ru1–N6	–	92.00(18)	89.0(2)	94.5(6)
N3–Ru1–Cl1	90.5(3)	–	–	–
N4–Ru1–N5	77.5(5)	78.77(18)	77.6(2)	77.1(5)
N4–Ru1–N6	–	178.08(17)	178.2(2)	176.6(6)
N4–Ru1–Cl1	175.8(3)	–	–	–
N5–Ru1–N6	–	101.86(18)	102.9(2)	99.5(6)
N5–Ru1–Cl1	100.5(4)	–	–	–
Ru1–N6–O1	–	–	122.7(5)	175.0(14)
Ru1–N6–O2	–	–	124.4(5)	–
O1–N6–O2	–	–	112.8(6)	–
N7–Ru2–N8	83.8(6)	–	–	–
N7–Ru2–N9	165.1(5)	–	–	–
N7–Ru2–N10	92.1(5)	–	–	–
N7–Ru2–N11	94.9(5)	–	–	–
N7–Ru2–Cl2	87.5(3)	–	–	–
N8–Ru2–N9	81.8(6)	82.30(18)	81.9(2)	–
N8–Ru2–N10	83.6(5)	163.7(2)	162.7(2)	–
N8–Ru2–N11	162.8(5)	88.77(17)	86.17(19)	–
N8–Ru2–N12	–	98.22(18)	97.6(2)	–
N8–Ru2–N13	–	89.68(18)	91.8(2)	
N8–Ru2–Cl2	93.8(4)	–	–	–
N9–Ru2–N10	90.4(5)	81.5(2)	80.84(19)	–
N9–Ru2–N11	100.0(5)	83.8(2)	83.10(19)	–
N9–Ru2–N12	–	162.1(2)	160.4(2)	–
N9–Ru2–N13	–	95.0(2)	101.40(19)	–
N9–Ru2–Cl2	89.3(3)	–	–	–
N10–Ru2–N11	79.2(5)	90.98(19)	92.34(19)	–
N10–Ru2–N12	–	97.6(2)	98.91(19)	–
N10–Ru2–N13	–	90.2(2)	91.0(2)	–
N10–Ru2–Cl2	177.4(4)	–	–	–
N11–Ru2–N12	–	78.3(2)	77.3(2)	–
N11–Ru2–N13	–	178.20(19)	174.8(2)	–
N11–Ru2–Cl2	103.3(3)	–	–	–
N12–Ru2–N13	–	102.8(2)	98.2(2)	–
Ru2–N13–O3	–	–	124.1(4)	–
Ru2–N13–O4	–	–	120.6(4)	–
O3–N13–O4	–	–	114.7(5)	–

Table 3
Electronic spectral data of the complexes in CH_3CN.

Complexes	λ [nm] (ε [M^{-1} cm^{-1}])
MePBITA	240.5(20674), 263(15181), 268.5(15358), 311(29698)
[**1**](PF_6)	253(19178), 323.5(20617), 429.5(7481), 519.5(5197)
[**2**](PF_6)$_2$	247.5(27561), 324(25628), 381(9559), 460(6391)
[**3**](PF_6)	249(21647), 324(21528), 387.5(7471), 480(4893)
[**4**](ClO_4)$_3$	249(22686), 261(24232), 325.5(13202), 382(4634)
[**4**](ClO_4)$_2$	252.5(28923), 270.5(23153), 324.5(21314), 381(7790), 463(5229)

Table 4
FT-IR vibrational frequencies.

Complexes	ν (NO) cm^{-1}	Ref
$[Ru(SBPy_3)(NO^+)]^{3+}$	1920	[11]
$[Ru(PaPy_3)(NO^+)]^{2+}$	1899	[11]
$[Ru(Py_3P)(NO^+)]^+$	1877	[11]
$[Ru(Py_3P)(NO^+)(Cl)]$	1862	[11]
$[Ru(MePBITA)(NO^+)]^{3+}$	1931	This work

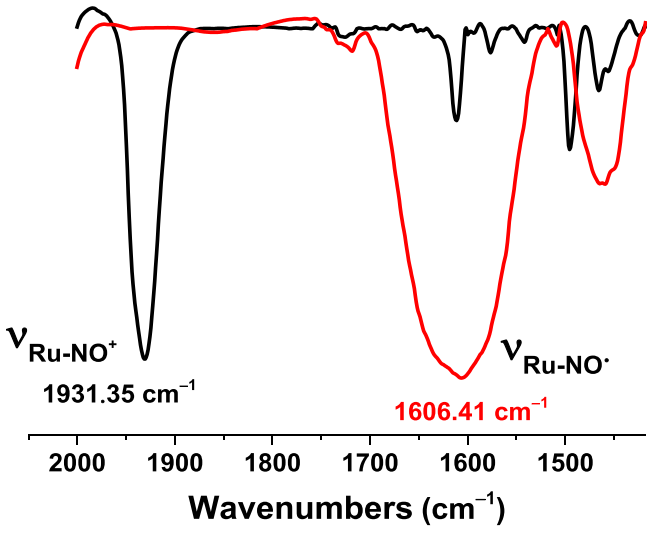

Fig. 6. FT-IR (solid) spectra of $[4]^{3+}$ and $[4]^{2+}$.

derivatized pyridyl benzimidazole ligand has increased NO stretching frequency significantly to 1931 cm^{-1}, suggesting the high moderately electrophilic character of NO. The strong σ-donor and π-acceptor character of MePBITA ligand helps to increase and stabilized the Ru–NO stretching frequency substantially. Thus, by introducing the chelating bidentate pyridine benzimidazole moiety has a significant impact on varying the stretching frequency of the Ru–NO complexes and therefore important photo physical properties of ruthenium nitrosyls expected to be nicely tuned. In earlier report it has been proven that ancillary ligands play an indispensable role for electrophilic character of the Ru–NO bond but this present report reveals how the appropriate designing of polypyridyl pentadentate ligand with improved electronic nature can help in the variation of Ru–NO stretching frequency. The stretching frequency of [**4**](ClO_4)$_3$ has been reduced largely from 1931 cm^{-1} to 1606 cm^{-1} via one-electron reduction (Fig. 6). Shift of stretching frequency (325 cm^{-1}) is because of occupancy of electron to the vacant π^* orbital of NO and eventually reduces the bond order. The respectable shift in ν_{NO} frequency, $\Delta\nu$ (solid) = 325 cm^{-1} by reducing [**4**](ClO_4)$_3$ to [**4**](ClO_4)$_2$ is mainly related with geometry change from linear Ru^{II}–NO^+ to most likely bent Ru^{II}–$NO^{\bullet}$ [38, 41].

3.3.4. Redox properties and EPR study

Due to the different electronic nature of the monodentate ligand coordination, the oxidation potentials of Ru(II)/(III) couples in acetonitrile at $E°_{298K}/V$ are observed at 0.546 V, 1.054 V and 0.801 V *vs* SCE (saturated calomel electrode) for [**1**](PF_6), [**2**](PF_6)$_2$ and [**3**](PF_6), respectively (Table 5, Fig. 7(a), (b), (c)). Systematic variation of the redox couples is witnessed in the order Cl^- < NO_2^- < CH_3CN. Due to the stronger ligand field strength of NO_2^- than Cl^- relatively larger value of Ru(II)/(III) couples is seen in [**3**](PF_6) than [**1**](PF_6). Similarly, the more positive potential value in [**2**](PF_6)$_2$ implies the additional stability of Ru(II) state, because of the combined effect of electrostatic nature and for the overall charge of $[2]^{2+}$ in comparison with $[3]^+$ / $[1]^+$ and the ligand field strength. The free ligand MePBITA is also redox active and the successive reductions are observed in the range of – 2.13 V to – 2.64 V. Correspondingly, in all of the complexes [**1**](PF_6), [**2**](PF_6)$_2$ and [**3**](PF_6) the ligand based reductions are observed in the range of – 1.45 V to – 2.56 V suggesting nice metal-ligand delocalization. Interestingly in the case of [**4**](ClO_4)$_3$ the Ru(II)/(III) couples in acetonitrile at $E°_{298K}/V$ are not observed within the experimental solvent potential window + 2 V *vs* SCE in CH_3CN due to the efficient stabilization of Ru(II) state by the powerful π–acidic chelating MePBITA ligand. In $[4]^{3+}$ the first reduction is found reversible while the second reduction is irreversible. The NO centered reductions for [**4**](ClO_4)$_3$ are appeared at + 0.27 V and – 0.76 V which can be assigned as $[Ru^{II}–NO^+]$ to $[Ru^{II}–NO^{\bullet}]$ and $[Ru^{II}–NO^{\bullet}]$ to $[Ru^{II}–NO^-]$, respectively (Fig. 7(d)). The isolation of intermediate complex [**4**](ClO_4)$_2$ has been successful due to the considerably large comproportionation constant, *Kc* ($10^{17.62}$) {RTln*Kc* = nF(ΔE)}; (ΔE = difference in potential between the NO centered reductions). Previously reported analogous ruthenium complexes exhibited the similar potential for $[Ru^{II}–NO^+]$ to $[Ru^{II}–NO^{\bullet}]$. In 2007 Mascharak et al. reported for the complexes $[Ru^{II}(SBPy_3)(NO^+)]^{3+}$, $[Ru^{II}(PaPy_3)(NO^+)]^{2+}$ and $[Ru^{II}(Py_3P)(NO^+)]^+$ the oxidation potentials are found to be 0.290 V, –0.225 V and –0.205 V, respectively [23] (Drawing of ligands, Supporting Information). The high positive charge associated with [**4**](ClO_4)$_3$ along with positive reduction potential further facilitated the isolation of [**4**](ClO_4)$_2$. To investigate the paramagnetic one-electron reduced [**4**](ClO_4)$_2$ radical complex, the X-band EPR spectrum was carried out, and the complex was found to be EPR active as anticipated for unpaired electron species with typical $\{RuNO\}^7$ EPR spectrum. The solid-state EPR spectrum of reduced nitrosyl [**4**](ClO_4)$_2$ at 298 K exhibited a broad signal with g = ~ 2.22 suggesting a substantial contribution of ruthenium and singly occupied MO of nitrosyl. The EPR spectrum of the reduced species [**4**](ClO_4)$_2$ arises due to the degree of M–N–O bending and a partial mixing of the frontier orbitals from the ruthenium ion and the close single-occupied molecular orbitals of NO. The similarity of the EPR parameters with those observed and previously reported is compatible with contributions of about 33 percent from the ruthenium and the rest 67 percent from the NO group to the SOMO which implies a mixed resonance formulation $\{Ru^I(NO^+)\} \leftrightarrow \{Ru^{II}(NO^{\bullet})\}$ [37,38].

3.4. Conversion of $[3]^+$ from $[4]^{3+}$

The electrophilic nature of Ru–NO bond towards nucleophiles largely depends on the environment of the coordinated ligand system in the complexes which is strongly associated with Ru(dπ) to NO(π^*) back bonding. Furthermore, the conversion of $[4]^{3+}$ to $[3]^+$ has been taken place when 1 mM of complex $[4]^{3+}$ in acetonitrile was treated with 0.5 M NaOH solution with subsequent prominent electrochemical change in the cyclic voltammogram (Fig. 9) [37]. This change in the potentials during the electrochemical conversion suggested the transformation to nitro derivative from $[4]^{3+}$ as the final product is identical to the synthesized $[3]^+$. The step-

Table 5
Redox potential values of complexes[a].

Complex	Couple			MePBITA reduction
	Ru^{III}/Ru^{II}	$Ru-NO^{+}\rightarrow Ru-NO^{\bullet}$	$Ru-NO^{\bullet}\rightarrow Ru-NO^{-}$	
[**1**](PF_6)	0.546	–	–	−1.63, −2.06, −2.30, −2.51
[**2**]$(PF_6)_2$	1.054	–	–	−1.45, −1.87, −2.15, −2.36
[**3**](PF_6)	0.801	–	–	−1.71, −2.04, −2.24, −2.56
[**4**]$(ClO_4)_3$	–	0.27	−0.76	–

[a] Potentials $E°_{298K/V}$ in volt (ΔE[mV]) versus SCE in CH_3CN/0.1 M $^{n}Bu_4NClO_4$ scan rate 100 mVs^{-1}.

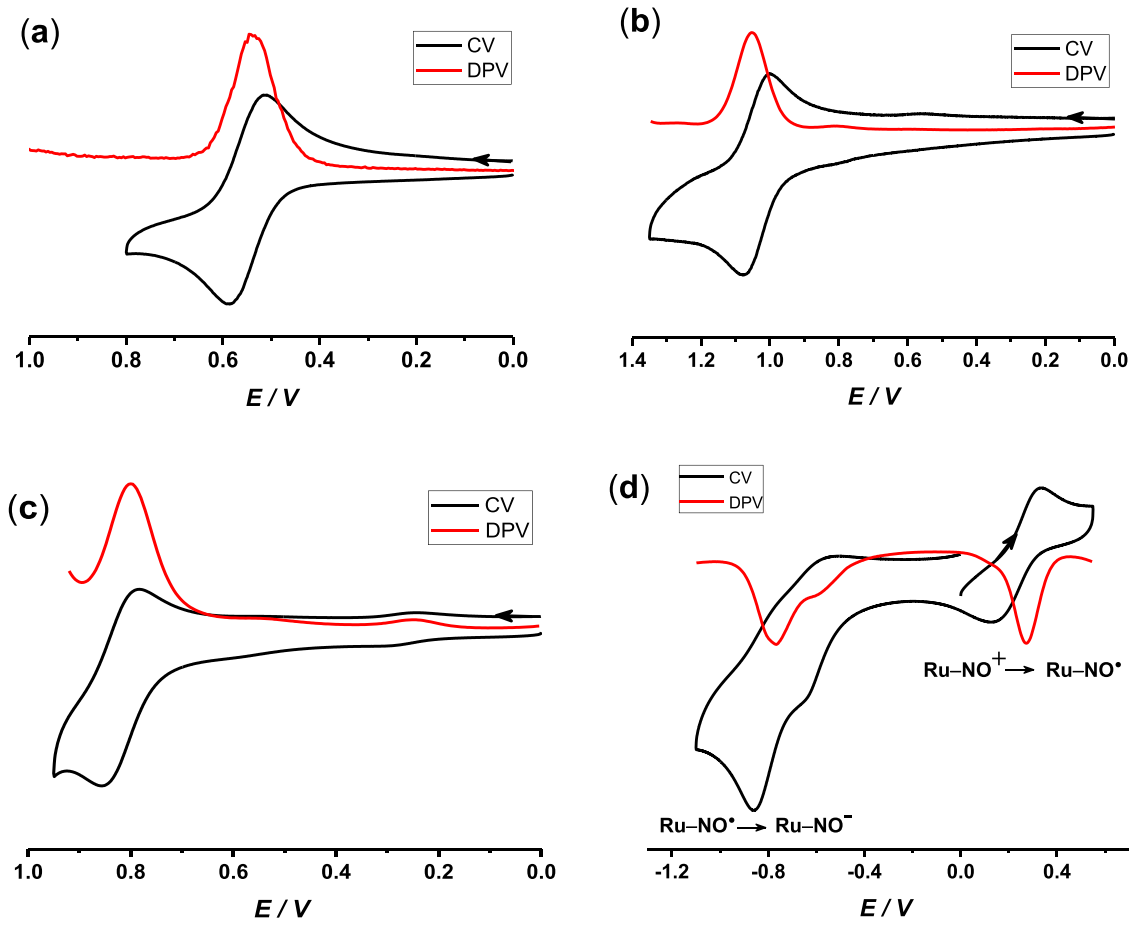

Fig. 7. Cyclic voltammograms and Differential pulse voltammograms of (a) [**1**](PF_6), (b) [**2**]$(PF_6)_2$, (c) [**3**](PF_6) and (d) [**4**]$(ClO_4)_3$ in CH_3CN/0.1M TBAP versus SCE, scan rate 100 mVs^{-1}.

wise electrochemical conversion of $[\mathbf{4}]^{3+}$ to $[\mathbf{3}]^{+}$ has been represented in Fig. 9.

The gradual disappearance of $[Ru^{II}-NO^{+}]$ to $[Ru^{II}-NO^{\bullet}]$ couple at ~ 0.27 V with concomitant formation of Ru(II)/Ru(III) couple at ~ 0.8 V clearly suggest the transformation of $[\mathbf{4}]^{3+}$ to $[\mathbf{3}]^{+}$ in the presence of sodium hydroxide base following the Eq. (1):

$$\left[Ru^{II}(MePBITA)\left(NO^{+}\right)\right]^{3+} + 2OH^{-} \rightleftharpoons \left[Ru^{II}(MePBITA)(NO_2)\right]^{+} + H_2O \quad (1)$$

The simultaneous decrease of the redox couple at ~ 0.27 V ($Ru^{II}-NO^{+}\rightarrow Ru^{II}-NO^{\bullet}$) corroborates the nucleophilic attack by OH^{-} to the corresponding orbital of NO(π^{*}) of $[\mathbf{4}]^{3+}$. The same conversion was monitored by UV-vis spectral change. The continuous progressive increasing band at 480 nm further confirms the formation of $[\mathbf{3}]^{+}$ from $[\mathbf{4}]^{3+}$ by comparing the spectra of the synthesized precursor nitro derivative $[\mathbf{3}]^{+}$ (Fig. S19).

3.5. Photo cleavage of Ru–NO bond in $[4](ClO_4)_3$ and $[4](ClO_4)_2$

Under normal ambient light in acetonitrile both the nitrosyl derivatives [**4**]$(ClO_4)_3$ and [**4**]$(ClO_4)_2$ are fairly stable. On the other hand when [**4**]$(ClO_4)_3$ and [**4**]$(ClO_4)_2$ in degassed acetonitrile solution were exposed to visible Xenon light (200 W), the Ru–NO cleavage took place readily and transformed to their solvated species $[\mathbf{2}]^{2+}$ with distinct color change to orange. Subsquently the formed $[\mathbf{2}]^{2+}$ was further confirmed by visual color change as well as spectral change in UV-vis analysis (Fig. 12). The light induced cleavage of $\{Ru^{II}-NO^{+}\}$ bond is progressing through the formation of intermediate species $\{Ru^{III}-NO^{\bullet}\}^{*}$ (S = 1 state) by the following Eq. (2) [12, 22, 43, 44].

$$\left\{Ru^{II}-NO^{+}\right\} + h\nu \rightarrow \left\{Ru^{III}-NO^{\bullet}\right\}^{*} \rightarrow \left\{Ru^{II}-CH_3CN\right\} + NO^{\bullet} \quad (2)$$

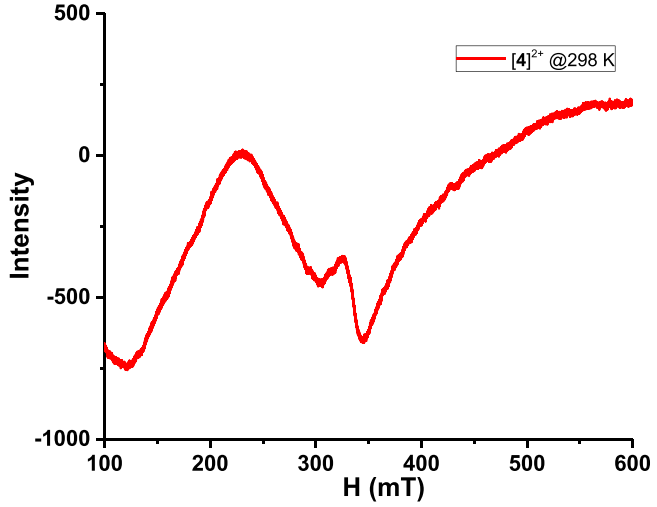

Fig. 8. The EPR spectrum of [**4**]$(ClO_4)_2$ in solid state at 298 K. Conditions for EPR spectra for complex [**4**]$(ClO_4)_2$ at 298 K; Center Field: 497.153 mT; Width: +/- = 500 mT; Microwave Frequency: 9.452 GHz.

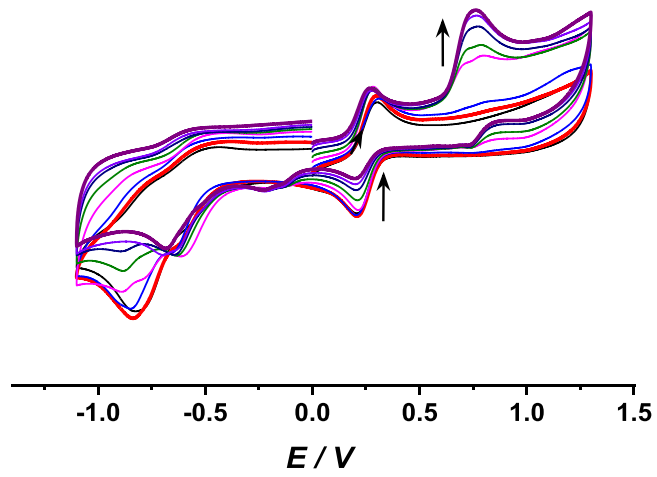

Fig. 9. Electrochemical conversion of $[\mathbf{4}]^{3+}$ to $[\mathbf{3}]^{+}$ in CH_3CN/0.1M TBAP versus SCE after sequential addition of 0.5 M NaOH, scan rate 100 mVs^{-1}.

The final product {Ru^{II}–CH_3CN} species was confirmed after photo-cleavage with the help of UV-vis analysis by comparing with the spectra of synthesized solvated species $[\mathbf{2}]^{2+}$. In case of $[\mathbf{4}]^{3+}$ the photo-cleavage of Ru–NO bond is performed for ~ 2 h but for the reduced radical species $[\mathbf{4}]^{2+}$ the same is ~ 80 min. Therefore, indicating under the same photolytic condition the cleavage of Ru^{II}–NO bond is much faster in $[\mathbf{4}]^{2+}$ compared to $[\mathbf{4}]^{3+}$ (Figs. 10–11).

The kinetic parameter for the visible light induced photo cleavage has been determined and the first-order rate constants for NO release have been found to be 8.99×10^{-3} min^{-1}; half-life ($t_{1/2}$) = 77 min and 3.84×10^{-2} min^{-1}; half-life ($t_{1/2}$) = 18 min for $[\mathbf{4}]^{3+}$ and $[\mathbf{4}]^{2+}$, respectively. However under similar photolytic condition in our very recent work the first-order rate constants was found 8.01×10^{-3} min^{-1}; half-life ($t_{1/2}$) = 86 min for $[Ru^{II}(antpy)(bpy)(NO^{+})](PF_6)_3$ and 3.27×10^{-2} min^{-1}; half-life ($t_{1/2}$) = 21 min for $[Ru^{II}(antpy)(bpy)(NO^{\bullet})](PF_6)_2$ [37], respectively suggesting superior photolabile nature of Ru–NO bond in the present case due to the unique ligand environment. Also $[Ru^{II}(tpy)(pdt)(NO^{\bullet})]^{2+}$ complex undergoes photorelease with very slow rate (k_{NO}) = 4.4×10^{-3} min^{-1}; half-life

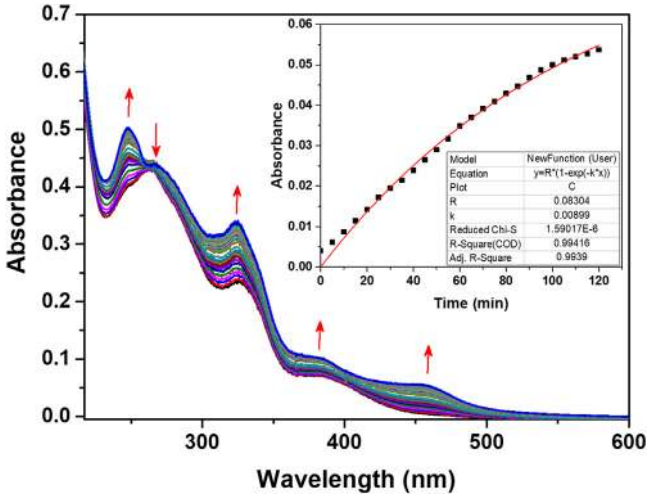

Fig. 10. Time evolution of the electronic spectrum (time interval 5 min) of the solution of $[\mathbf{4}]^{3+}$ (concentration 1.0×10^{-5} M in CH_3CN) under the exposure of visible light Xenon 200 W. Inset shows the plot of absorbance versus time plot at 460 nm corresponding to the solvate species.

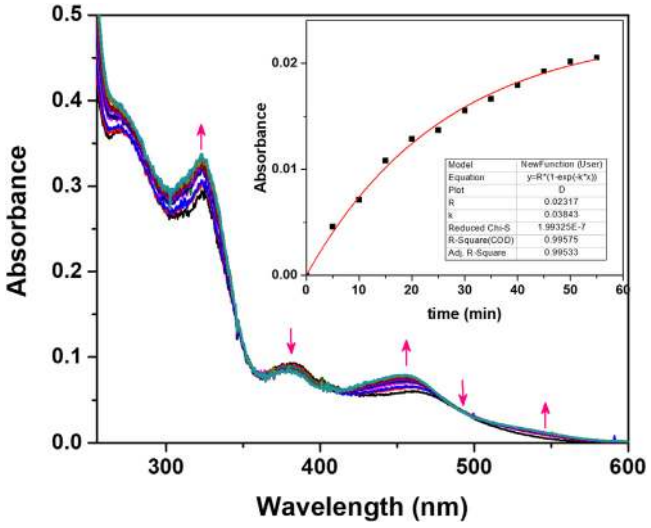

Fig. 11. Time evolution of the electronic spectrum (time interval 5 min) of the solution of $[\mathbf{4}]^{2+}$ (concentration 1.0×10^{-5} M in CH_3CN) under the exposure of visible light Xenon 200 W. Inset shows the plot of absorbance versus time plot at 460 nm corresponding to the solvate species.

($t_{1/2}$) = 157 min [42]. Interestingly, Ru–NO bond cleavage did not occur in $[Ru^{II}(tpy)(pip)(NO^{+})]^{3+}$ complex when it was exposed with higher energy 350 W visible xenon light, but the reduced $[Ru^{II}(tpy)(pip)(NO^{\bullet})]^{2+}$ was susceptible for the photocleavage with the rate (k_{NO}) = 2.0×10^{-1} min^{-1}; half-life ($t_{1/2}$) = 3.5 min [38].

3.6. Scavenging of photo-liberated NO by myoglobin (Mb)

After photolysis of $[\mathbf{4}]^{3+}$ and $[\mathbf{4}]^{2+}$, the liberated NO was passed through the deoxygenated (degassed with argon atmosphere) aqueous solution of reduced myoglobin which was freshly prepared (following standard procedure and with excess sodium dithionite) an intense band at λ_{max} = 420 nm was observed in the electronic spectra [45]. This characteristic peak, due to Fe^{II}–NO bonding in myoglobin confirmed the formation of Mb–NO adduct. In the electronic spectra, myoglobin and reduced myoglobin exhibited strong peaks at 408 nm (Soret peak) and 432 nm, respectively (Fig. 13) [13,20].

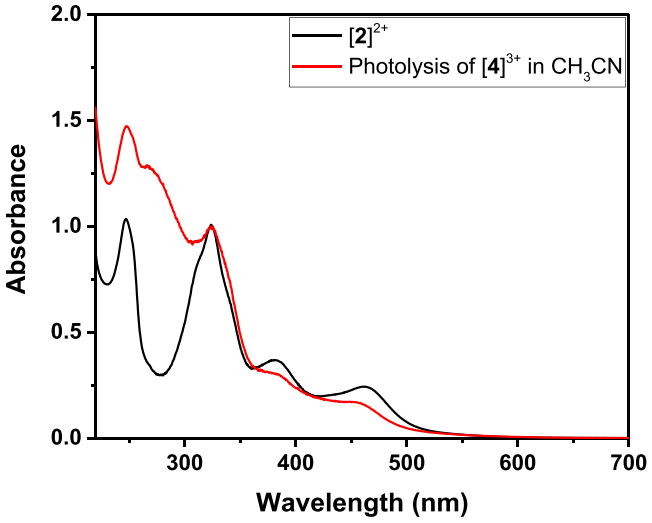

Fig. 12. The electronic spectrum of the final spectrum after photolysis in CH_3CN from $[4]^{3+}$ and isolated spectrum $[2]^{2+}$ in CH_3CN.

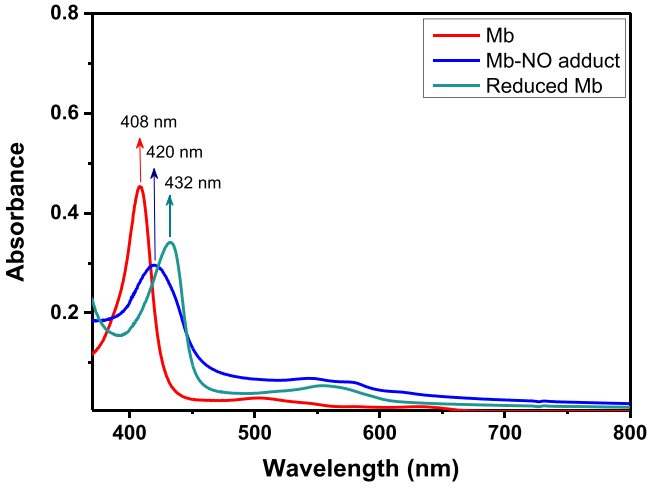

Fig. 13. UV-vis spectra of myoglobin (red) reduced myoglobin (green) and Mb-NO adduct (blue). The spectra were recorded in milli-Q water at room temperature.

3.7. Live-cell and fluorescence imaging

Photo-cytotoxicity of all the ruthenium derivatives was determined in prostate carcinoma cells; VCaP and 22Rv1, and lung carcinoma cells; A549. Initially, the cells were treated with multiple concentrations (0.5, 1, 2.5, 5, 10, 15, 20, 25, and 50 μM) of various complexes ([**1**](PF_6), [**2**]$(PF_6)_2$, [**3**](PF_6), [**4**]$(ClO_4)_3$ and [**4**]$(ClO_4)_2$) for 6 h in dark and were exposed to visible light for 15 min using a Xenon (200 W) visible light bulb. The compounds [**4**]$(ClO_4)_3$ and [**4**]$(ClO_4)_2$ exhibited cell death upon their treatment in VCaP and 22Rv1 cells at final concentrations of 50 μM and 10 μM, respectively as a number of viable cells observed after treatment at indicated concentrations was far lesser than the viable cells observed after treatment with lower concentrations of nitrosyl compounds, and most of these viable cells had lost their normal morphology. Also, both the nitrosyl compounds [**4**]$(ClO_4)_3$ and [**4**]$(ClO_4)_2$ were highly toxic to A549 cells at 5 μM and 1 μM concentrations, respectively (Fig. 15). No significant cell death was observed on photo-exposure of VCaP and 22Rv1 cells treated with 50 μM, and A549 with 5 μM of compounds [**1**](PF_6), [**2**]$(PF_6)_2$, and [**3**](PF_6) (Fig. S20). These effects were observed due to oxidative stress caused by unregulated release of highly reactive NO into the cells upon [**4**]$(ClO_4)_3$ and [**4**]$(ClO_4)_2$ treatment. Moreover, cytotoxicity was not observed prior to irradiation in cells treated with any of the nitrosyl complexes. Similar observations were obtained upon staining the cells with a fluorescent DNA stain DAPI (4,6-diamidino-2-phenylindole). DNA fragmentation and nuclear degradation were observed in the cells treated with [**4**]$(ClO_4)_3$ and [**4**]$(ClO_4)_2$ upon irradiation whereas no significant aberration was observed in the treated cells without irradiation (Fig. 14). Consistent with the above results, significant cell death was observed on crystal violet staining of the cells treated with [**4**]$(ClO_4)_3$ and [**4**]$(ClO_4)_2$ on photo-exposure (Fig. S21). Cytotoxicity was not observed in cells that were not exposed to visible light and also, in the cells treated with [**1**](PF_6), [**2**]$(PF_6)_2$, and [**3**](PF_6) even after photo-exposure. It can be inferred from our observations that nitrosyl complexes [**4**]$(ClO_4)_3$ and [**4**]$(ClO_4)_2$ are toxic to VCaP, 22Rv1, and A549 cells on visible light irradiation only, and remain non-toxic to the cells without irradiation. Overall, our results suggest that complexes [**4**]$(ClO_4)_3$ and [**4**]$(ClO_4)_2$ possess substantial photo-cytotoxic behavior and exhibit excellent photoactivation properties.

Table 6
IC_{50} values of nitrosyl complexes and *cis*-platin in various human cell lines.

Cell Lines	IC_{50} (μM)			
	[**4**]$(ClO_4)_3$	[**4**]$(ClO_4)_2$	*cis*-platin	Ref
VCaP	29.74	4.42	––	––
22Rv1	29.96	6.88	24	[47]
A549	2.24	0.12	31.25	[48]

3.8. Cell cytotoxicity in cancer cell lines

An MTT (3-(4,5-dimethylthiazol-2-yl)-2,5-diphenyltetrazolium bromide) assay was performed to understand the photo-activation of all the ruthenium derivatives in VCaP, 22Rv1, and A549 cells [34]. This assay utilizes the metabolic activity of cells wherein the oxidoreductase enzymes present in the mitochondria of the cells carry out the conversion of yellow-colored MTT reagent to colorless formazan crystals in live cells. Hence, this assay determines cell viability and cytotoxicity [45]. Later, these crystals are dissolved in an MTT solvent to give violet-colored complex which was measured at 595 nm. We have examined the viability of VCaP, 22Rv1, and A549 cells upon photoactivation of all ruthenium derivatives. Treatment of the cells with [**1**](PF_6), [**2**]$(PF_6)_2$, and [**3**](PF_6) did not show any significant cell death upon irradiation, while the cells treated with [**4**]$(ClO_4)_3$ and [**4**]$(ClO_4)_2$ exhibit substantial cytotoxicity upon irradiation using a Xenon (200 W) visible light bulb (Fig. 15). Observed IC_{50} values of [**4**]$(ClO_4)_3$ and [**4**]$(ClO_4)_2$ in VCaP are 29.74 and 4.42 μM, in 22Rv1 are 29.96 and 6.88 μM, and in A549 are 2.24 and 0.12 μM, respectively (Table 6). These values are significantly lower compared to earlier reported similar systems and are remarkable towards the newer generation of photoactive metal nitrosyls. Ruthenium nitrosyl complex *cis*-$[Ru(NO)(bpy)_2(4\text{-pic})](PF_6)_3$ are known to induce apoptosis in hepatocarcinoma cells by activating caspases 9 and 3 [46]. In our previous studies, substantial cytotoxicity was observed in VCaP cells ($IC_{50} \sim 8.97$ μM) on nitrosyl compound $[Ru^{II}(antpy)(bpy)(NO^+)](PF_6)_3$ treatment upon similar visible light irradiation [37]. The IC_{50} values observed for this study in 22Rv1 and A549 cells are comparable to that of *cis*-platin (Table 6) [47,48]. Thus, our results suggest that [**4**]$(ClO_4)_3$ and [**4**]$(ClO_4)_2$ are exceptionally toxic to VCaP, 22Rv1, and A549 cells upon photoactivation with visible light irradiation. Therefore, with proper ligand design, MePBITA can easily aid the release of NO under mild

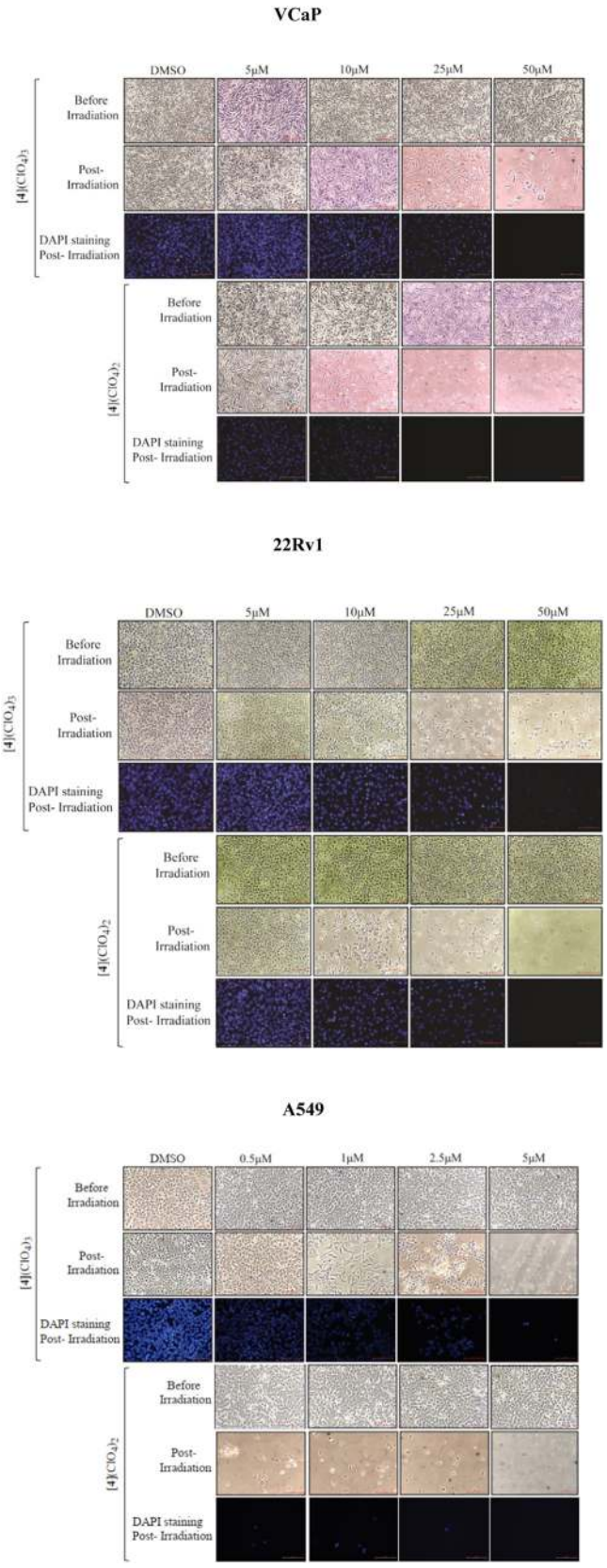

Fig. 14. Images of VCaP, 22Rv1 and A549 cells upon treatment of nitrosyl complexes [**4**]$(ClO_4)_3$, and [**4**]$(ClO_4)_2$. Bright-field images and fluorescence images of VCaP, 22Rv1 and A549 cells treated with [**4**]$(ClO_4)_3$ and [**4**]$(ClO_4)_2$ captured before and after irradiation.

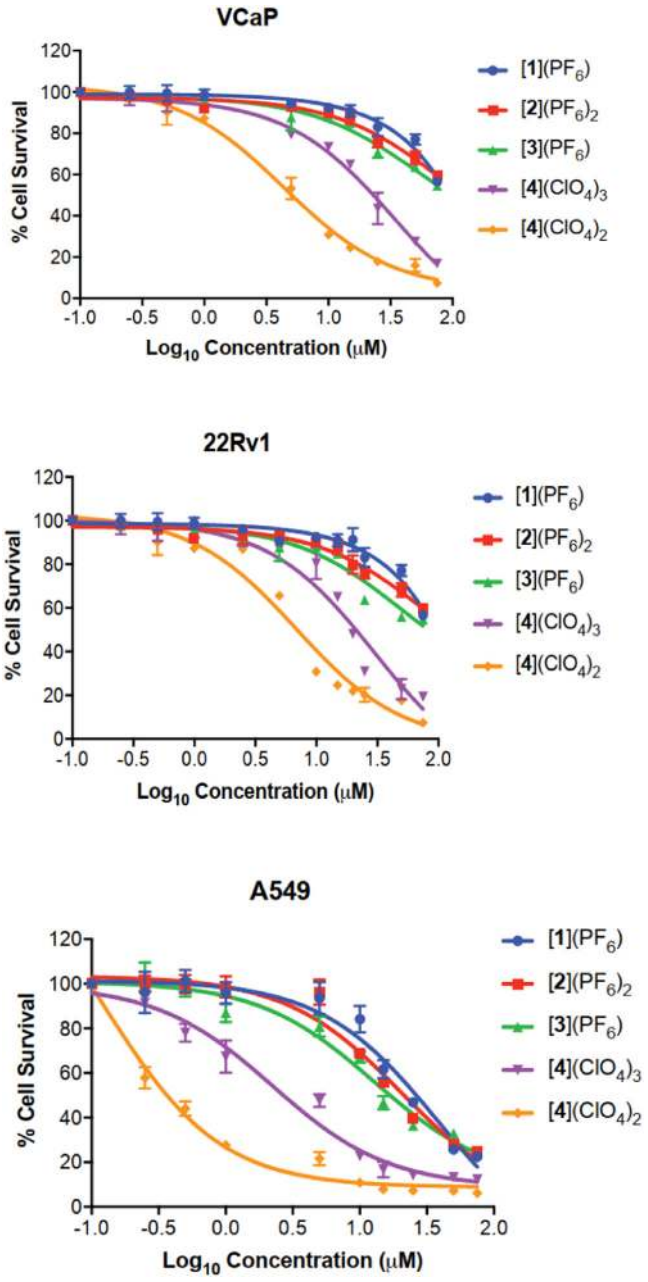

Fig. 15. Effect of visible light exposure on VCaP, 22Rv1 and A549 cancer cell lines in the presence of $[\mathbf{1}]^{+}$, $[\mathbf{2}]^{2+}$, $[\mathbf{3}]^{+}$, $[\mathbf{4}]^{3+}$ and $[\mathbf{4}]^{2+}$.

postexposure and consequently improve the antineoplastic behavior.

4. Conclusion

In summary the present work reveals the electron rich pentadentate ligand MePBITA with the molecular framework $[Ru^{II}(MePBITA)(NO)]^{n+}$ (n = 3, 2) and MePBITA = 1-(6-(1-methyl-1H-benzo[d]imidazol-2-yl)pyridin-2-yl)-N,N-bis(pyridin-2-ylmethyl)methanamine) permits the isolation of both the redox states of nitrosyls with Enemark–Feltham notation $\{RuNO\}^6$, $[\mathbf{4}]^{3+}$ (n = 3), and $\{RuNO\}^7$, $[\mathbf{4}]^{2+}$ (n = 2). Along with the free ligand, the redox and spectral properties for all the complexes have been systematically explored. The one-electron reduced radical species have been synthesized chemically as well as electrochemically. Both the redox states can be reversibly interconverted via single

electron transfer. Single crystal X-ray structure of the complexes [**1**](PF_6), [**2**](PF_6)$_2$, [**3**](PF_6) and [**4**](ClO_4)$_3$ have been successfully determined by X-ray diffraction study. The conversion of nitro derivative [**3**]$^+$ from nitrosyl species [**4**]$^{3+}$ was examined with the addition of 0.5 M NaOH solution both electrochemically and spectrophotometrically. Ru−NO stretching frequency observed at 1931 cm^{-1} for [**4**](ClO_4)$_3$ suggests a moderately electrophilic character of NO. The remarkable shift of ν (NO) (solid) ($\Delta\nu$ = 325 cm^{-1}) can be explained by the NO centered reduction, moving from [**4**]$^{3+}$ to [**4**]$^{2+}$ with the bonding changes from linear {RuNO}^{6} to most probably bent {RuNO}^{7}. Both the nitrosyl derivatives NO^+ and $NO^\bullet$ are prone to photorelease on exposure to visible Xenon light (200 W) irradiation suggesting the suitability of metallodrug for photochemotherapy (PCT) in the photo-therapeutic window. The photo liberated NO has been scavenged by biologically relevant target protein reduced myoglobin as Mb−NO adduct. The antineoplastic behavior of photoreleased NO is determined in three different cancer cell lines, VCaP, 22Rv1 and A549. The live-cell imaging and viability experiments reveal that [**4**](ClO_4)$_3$ and [**4**](ClO_4)$_2$ induce significant cytotoxicity in VCaP, 22Rv1 and A549 cells upon photoactivation using visible light. Photoactivation of nitrosyl compounds triggers the release of NO, which induces oxidative damage inside the cells leading to apoptosis. Taken together, our study underscores the importance of using MePBITA coordinated ruthenium nitrosyl complexes as potential PCT agents for the treatment of a wide variety of cancers. This study will open a new window for the future design of PCT agents in the photo-therapeutic region.

Declaration of Competing Interest

There are no conflicts to declare.

Acknowledgment

Financial support received from SERB, project no. ECR/2016/000382 (Somnath Maji and fellowship to S.K.), Council of Scientific and Industrial Research (CSIR) (fellowship to B.G., A.M. and K.S.) and IIT Hyderabad are gratefully acknowledged for the financial support. S.K. and P.G. acknowledge fellowship support from MoE. Ashish Misra acknowledges financial support from SERB (project no. ECR/2017/002544).

Supplementary materials

Supplementary material associated with this article can be found, in the online version, at doi:10.1016/j.molstruc.2022.133419.

References

[1] J.S. Stamler, D.J. Singel, J. Loscalzo, Biochemistry of nitric oxide and its redox-activated forms, Science 258 (1992) 1898–1902.
[2] B. Brüne, The Biology of nitric oxide, Part 7, Cell Death Differ. 8 (2001) 106–108.
[3] J.A. McCleverty, Chemistry of nitric oxide relevant to biology, Chem. Rev. 104 (2004) 403–418.
[4] Z.J. Tonzetich, L.E. McQuade, S.J. Lippard, Detecting and understanding the roles of nitric oxide in biology, Inorg. Chem. 49 (2010) 6338–6348.
[5] H.P. Monteiro, E.G. Rodrigues, A.K.C. Amorim Reis, L.S. Longo, F.T. Ogata, A.I.S. Moretti, P.E. da Costa, A.C.S. Teodoro, M.S. Toledo, A. Stern, Nitric oxide and interactions with reactive oxygen species in the development of melanoma, breast, and colon cancer: a redox signaling perspective, Nitric Oxide 89 (2019) 1–13.
[6] N. Marchenko, P.G. Lacroix, V. Bukhanko, M. Tassé, C. Duhayon, M. Boggio–Pasqua, I. Malfant, Multistep photochemical reactions of polypyridine-based ruthenium nitrosyl complexes in dimethylsulfoxide, Molecules 25 (2020) 2205.
[7] R.H. Ritchie, G.R. Drummond, C.G. Sobey, T.M. De Silva, B.K. Kemp-Harper, The opposing roles of NO and oxidative stress in cardiovascular disease, Pharmacol. Res. 116 (2017) 57–69.
[8] C. Farah, L.Y.M. Michel, J.-L. Balligand, Nitric oxide signalling in cardiovascular health and disease, Nat. Rev. Cardiol. 15 (2018) 292–316.
[9] A. Quillon, B. Fromy, R. Debret, Endothelium microenvironment sensing leading to nitric oxide mediated vasodilation: A review of nervous and biomechanical signals, Nitric Oxide 45 (2015) 20–26.
[10] S. Huerta, Nitric oxide for cancer therapy, Future Sci. OA. 1 (1) (2015) 44.
[11] S. Huerta, S. Chilka, B. Bonavida, Nitric oxide donors: novel cancer therapeutics, Int. J. Oncol. 33 (2008) 909–927.
[12] N.L. Fry, P.K. Mascharak, Photoactive ruthenium nitrosyls as NO donors: how to sensitize them toward visible light, Acc. Chem. Res. 44 (2011) 289–298.
[13] A.C. Merkle, A.B. McQuarters, N. Lehnert, Synthesis, spectroscopic analysis and photolabilization of water-soluble ruthenium(III)–nitrosyl complexes, Dalton Trans, 41 (2012) 8047–8059.
[14] K. Ghosh, S. Kumar, R. Kumar, Ruthenium–nitrosyl complexes derived from ligands containing two carboxylate functional groups and studies on the photolability of coordinated NO, Eur. J. Inorg. Chem. (2014) 1454–1461.
[15] K. Ghosh, R. Kumar, K. Kumar, A. Ratnam, U.P. Singh, Reactivity of nitric oxide with ruthenium complexes derived from bidentate ligands: structure of a ruthenium nitrosyl complex, photoinduced generation and estimation of nitric oxide, RSC Adv. 4 (2014) 43599–43605.
[16] M.H. Al-Afyouni, T.N. Rohrabaugh, K.F. Al-Afyouni, C. Turro, New Ru(II) photocages operative with near-IR light: new platform for drug delivery in the PDT window, Chem. Sci. 9 (2018) 6711–6720.
[17] A.K. Patra, J.M. Rowland, D.S. Marlin, E. Bill, M.M. Olmstead, P.K. Mascharak, Iron nitrosyls of a pentadentate ligand containing a single carboxamide group: syntheses, structures, electronic properties, and photolability of NO, Inorg. Chem. 42 (2003) 6812–6823.
[18] T.C. Berto, A.L. Speelman, S. Zheng, N. Lehnert, Mono- and dinuclear non-heme iron–nitrosyl complexes: models for key intermediates in bacterial nitric oxide reductases, Coord. Chem. Rev. 257 (2013) 244–259.
[19] A.B. McQuarters, J.W. Kampf, E.E. Alp, M. Hu, J. Zhao, N. Lehnert, Ferric heme-nitrosyl complexes: kinetically robust or unstable intermediates? Inorg. Chem. 56 (2017) 10513–10528.
[20] K. Ghosh, R. Kumar, S. Kumar, J.S. Meena, Syntheses, structures and properties of ruthenium complexes of tridentate ligands: isolation and characterization of a rare example of ruthenium nitrosyl complex containing {RuNO}^{5} moiety, Dalton Trans. 42 (2013) 13444–13452.
[21] E. Tfouni, D.R. Truzzi, A. Tavares, A.J. Gomes, L.E. Figueiredo, D.W. Franco, Biological activity of ruthenium nitrosyl complexes, Nitric Oxide 26 (2012) 38–53.
[22] P. Labra-Vázquez, M. Bocé, M. Tassé, S. Mallet-Ladeira, P.G. Lacroix, N. Farfán, I. Malfant, Chemical and photochemical behavior of ruthenium nitrosyl complexes with terpyridine ligands in aqueous media, Dalton Trans. 49 (2020) 3138–3154.
[23] M.J. Rose, A.K. Patra, E.A. Alcid, M.M. Olmstead, P.K. Mascharak, Ruthenium nitrosyls derived from polypyridine ligands with carboxamide or imine nitrogen donor(s): isoelectronic complexes with different NO photolability, Inorg. Chem. 46 (2007) 2328–2338.
[24] Z. Liu, C. Zhang, Y. Li, Z. Wu, F. Qian, X. Yang, W. He, X. Gao, Z. Guo, A Zn^{2+} fluorescent sensor derived from 2-(Pyridin-2-yl)benzoimidazole with ratiometric sensing potential, Org. Lett. 11 (2009) 795–798.
[25] Z. Liu, C. Zhang, W. He, Z. Yang, X. Gao, Z. Guo, A highly sensitive ratiometric fluorescent probe for Cd^{2+} detection in aqueous solution and living cells, Chem. Commun. 46 (2010) 6138–6140.
[26] Y. Zhang, F.Liu Yang, K. Li, Fluorescent sensor for imidazole derivatives based on monomer−dimer equilibrium of a zinc porphyrin complex in a polymeric film, Anal. Chem. 76 (2004) 7336–7345.
[27] J. Sisko, A.J. Kassick, M. Mellinger, J.J. Filan, A. Allen, M.A. Olsen, An investigation of imidazole and oxazole syntheses using aryl-substituted TosMIC reagents, J. Org. Chem. 65 (2000) 1516–1524.
[28] B. Armitage, Photocleavage of nucleic acids, Chem. Rev. 98 (1998) 1171–1200.
[29] W.K. Pogozelski, T.D. Tullius, Oxidative strand scission of nucleic acids: routes initiated by hydrogen abstraction from the sugar moiety, Chem. Rev. 98 (1998) 1089–1108.
[30] C. Tu, Y. Shao, N. Gan, Q. Xu, Z. Guo, Oxidative DNA Strand scission induced by a trinuclear Copper(II) complex, Inorg. Chem. 43 (2004) 4761–4766.
[31] J.H. Enemark, R.D. Feltham, Principles of structure, bonding, and reactivity for metal nitrosyl complexes, Coord. Chem. Rev. 13 (1974) 339–406.
[32] G.M. Sheldrick, Crystal structure refinement with SHELXL, Acta Crystallogr. Sect. C Struct. Chem. 71 (2015) 3–8.
[33] O.V. Dolomanov, L.J. Bourhis, R.J. Gildea, J.A.K. Howard, H. Puschmann, OLEX2: a complete structure solution, refinement and analysis program, J. Appl. Crystallogr. 42 (2009) 339–341.
[34] A. Muley, K.S. Karumban, P. Gupta, S. Kumbhakar, B. Giri, R. Raut, A. Misra, S. Maji, Synthesis, structure, spectral, redox properties and anti-cancer activity of Ruthenium(II) Arene complexes with substituted Triazole Ligands, J. Organomet. Chem. 954–955 (2021) 122074.
[35] B. Chazotte, Labeling nuclear DNA with Hoechst 33342, Cold Spring Harb. Protoc. (2011) pdb.prot5557.
[36] J. Pitarch López, F.W. Heinemann, R. Prakash, B.A. Hess, O. Horner, C. Jeandey, J.-L. Oddou, J.-M. Latour, A. Grohmann, Iron carbonyl, nitrosyl, and nitro complexes of a tetrapodal pentadentate amine ligand: synthesis, electronic structure, and nitrite reductase-like reactivity, Chem. – Eur. J. 8 (2002) 5709–5722.
[37] B. Giri, T. Saini, S. Kumbhakar, K.S. K, A. Muley, A. Misra, S. Maji, Near-IR light-induced photorelease of nitric oxide (NO) on ruthenium nitrosyl complexes: formation, reactivity, and biological effects, Dalton Trans. 49 (2020) 10772–10785.
[38] S. Maji, B. Sarkar, M. Patra, A.K. Das, S.M. Mobin, W. Kaim, G.K. Lahiri, Formation, reactivity, and photorelease of metal bound nitrosyl in

[Ru(trpy)(L)(NO)]n+ (trpy=2,2′:6′,2′′-Terpyridine, L=2-Phenylimidazo[4,5-f]1, 10-phenanthroline), Inorg. Chem. 47 (2008) 3218–3227.
[39] B. Giri, S. Kumbhakar, K. Kalai Selvan, A. Muley, S. Maji, Formation, reactivity, photorelease, and scavenging of NO in ruthenium nitrosyl complexes, Inorg. Chim. Acta 502 (2020) 119360.
[40] B. Giri, S. Kumbhakar, K.S. K, A. Muley, S. Maji, Ruthenium nitrosyl complexes with the molecular framework [RuII(dmdptz)(bpy)(NO)]n+ (dmdptz: N, N -dimethyl-4,6-di(pyridin-2-yl)-1,3,5-triazin-2-amine and bpy: 2,2′-bipyridine). Electronic structure, reactivity aspects, photorelease, and scavenging of NO, New J. Chem. 44 (2020) 18732–18744.
[41] S. Sarkar, B. Sarkar, N. Chanda, S. Kar, S.M. Mobin, J. Fiedler, W. Kaim, G.K. Lahiri, Complex Series [Ru(tpy)(dpk)(X)]n+ (tpy=2,2′:6′,2′′-Terpyridine; dpk=2,2′-Dipyridyl Ketone; X=Cl−, CH3CN, NO2−, NO+, NO•, NO−): Substitution and Electron Transfer, Structure, and Spectroscopy, Inorg. Chem. 44 (2005) 6092–6099.
[42] S. Maji, C. Chatterjee, S.M. Mobin, G.K. Lahiri, Synthesis and Spectro–electrochemical Aspects of [RuII(trpy)(pdt)(X)]n+ (trpy=2,2′:6′,2′′-Terpyridine, pdt=5,6-Diphenyl-3-pyridyl-as-triazine, X=Cl−, CH3CN, NO2−, NO+, NO•) – Electrophilicity of RuII–NO+ and Photolability of Ru^{II}–$NO^{\bullet}$, Eur. J. Inorg. Chem. (2007) 3425–3434.
[43] N.L. Fry, B.J. Heilman, P.K. Mascharak, Dye-Tethered Ruthenium nitrosyls containing planar dicarboxamide tetradentate N4 ligands: effects of in-plane ligand twist on NO photolability, Inorg. Chem. 50 (2011) 317–324.
[44] M. Roose, M. Tassé, P.G. Lacroix, I. Malfant, Nitric oxide (NO) photo-release in a series of ruthenium–nitrosyl complexes: new experimental insights in the search for a comprehensive mechanism, New J. Chem. 43 (2019) 755–767.
[45] G.M. Halpenny, M.M. Olmstead, P.K. Mascharak, Incorporation of a designed ruthenium nitrosyl in PolyHEMA hydrogel and light-activated delivery of NO to myoglobin, Inorg. Chem. 46 (2007) 6601–6606.
[46] F.P. Rodrigues, Z.A. Carneiro, P. Mascharak, C. Curti, R.S.da Silva, Incorporation of a ruthenium nitrosyl complex into liposomes, the nitric oxide released from these liposomes and HepG2 cell death mechanism, Coord. Chem. Rev. 306 (2016) 701–707.
[47] M. Raudenska, M. Kratochvilova, T. Vicar, J. Gumulec, J. Balvan, H. Polanska, J. Pribyl, M. Masarik, Cisplatin enhances cell stiffness and decreases invasiveness rate in prostate cancer cells by actin accumulation, Sci. Rep. 9 (2019), doi:10.1038/srep19449.
[48] A. Kaplan, G.A. Ciftci, H.M. Kutlu, The apoptotic and genomic studies on A549 cell line induced by silver nitrate, Tumor Biol 39 (2017), doi:10.1016/j.ccr.2015.03.028.